We are IntechOpen,
the world's leading publisher of
Open Access books
Built by scientists, for scientists

6,900
Open access books available

185,000
International authors and editors

200M
Downloads

154
Countries delivered to

Our authors are among the

TOP 1%
most cited scientists

12.2%
Contributors from top 500 universities

CLARIVATE ANALYTICS
BOOK CITATION INDEX
INDEXED

WEB OF SCIENCE™

Selection of our books indexed in the Book Citation Index
in Web of Science™ Core Collection (BKCI)

Interested in publishing with us?
Contact book.department@intechopen.com

Numbers displayed above are based on latest data collected.
For more information visit www.intechopen.com

Planar Heterostructures Based on Graphene

Pavel V. Ratnikov and Andrei P. Silin

Additional information is available at the end of the chapter

Abstract

We investigate a planar heterostructures based on gapless graphene and its gap modifications such as a single single heterojunction, a quantum well, and a superlattice. We focus on electron properties of these heterostructures within the envelope wave functions. A new phenomena such as valley-polarized currents along the heterojunction and a pseudospin splitting of an energy spectrum in quantum wells are predicted.

Keywords: Graphene, planar heterostructures, pseudospin splitting, interface states, minibands.

1. Introduction

The creation of graphene, a monolayer of carbon atoms forming a regular hexagonal lattice [1–3], has stimulated extensive experimental and theoretical studies along various lines of research. Graphene's unique properties make it a promising material for a new generation of carbon-based nanoelectronic devices. In particular, carrier mobility in graphene amounts to $2 \cdot 10^5$ cm^2/(V s), and ballistic transport is possible on a submicrometer scale [4, 5].

Over a few past years, numerous theoretical and experimental results have been reported on electronic properties of nanometer-wide ribbons of graphene (nanoribbons). Among the first were studies of electronic states of graphene nanoribbons using the Dirac equation under appropriate boundary conditions [6, 7]. The electronic properties of a graphene nanoribbon strongly depend on its size and edge geometry [8]. In terms of transport properties, graphene nanoribbons are highly reminiscent of carbon nanotubes [9, 10] since free carrier motion inside them is also one-dimensional.

A field-effect transistor (FET) based on a 2 nm wide, 236 nm long graphene nanoribbon was fabricated in a recent study [11] (nanoribbons of widths between 10 and 60 nm were

also studied). The graphene nanoribbon was made narrow enough to open a gap of width required for room-temperature transistor operation. However, it is less compact than the graphene quantum-dot transistor 30 nm in diameter discussed in [12].

The results of paper [13] confirm that graphene devices exhibit very high electronic mobility μ on a hexagonal boron nitride (h-BN) substrates, graphene devices on WS_2 substrates (G/WS_2) are equally promising for high quality electronic transport $\mu \sim 3.8 \times 10^4$ cm^2/(V s) at room temperature, followed by G/MoS_2 $\mu \sim 10^4$ cm^2/(V s) and G/GaSe $\mu \sim 2.2 \times 10^3$ cm^2/(V s). However, authors of [13] observed a significant asymmetry in electron and hole conduction in G/WS_2 and G/MoS_2 heterostructures, most likely due to the presence of sulphur vacancies in the substrate crystals.

Heterogeneous engineering of two-dimensional layered materials, including metallic graphene and semiconducting transition metal dichalcogenides, presents an exciting opportunity to produce highly tunable electronic and optoelectronic systems. In order to engineer pristine layers and their interfaces, epitaxial growth of such heterostructures is required. We report the direct growth of crystalline, monolayer tungsten diselenide (WSe_2) on epitaxial graphene (EG) grown from silicon carbide. Vertical transport measurements across the WSe_2/EG heterostructure provides evidence that an additional barrier to carrier transport beyond the expected WSe_2/EG band offset exists due to the interlayer gap [14].

The integration of graphene and other atomically flat, two-dimensional materials has attracted much interest and been materialized very recently. An in-depth understanding of transport mechanisms in such heterostructures is essential. The vertically stacked graphene-based heterostructure transistors were manufactured to elucidate the mechanism of electron injection at the interface [15]. In a careful analysis of current-voltage characteristics, an unusual decrease in the effective Schottky barrier height and increase in the ideality factor were observed with decreasing temperature. A model of thermionic emission with a Gaussian distribution of barriers was able to precisely interpret the conduction mechanism.

The intrinsic performance of vertical and lateral graphene-based heterostructure FETs have been theoretically investigated in [16]. Authors focused on three recently proposed graphene-based transistors, that in experiments have exhibited large current modulation. The analysis is based on device simulations including the self-consistent solution of the electrostatic and transport equations within the non-equilibrium Green's function formalism. It was shown that the lateral heterostructure transistor has the potential to outperform the graphene-based technology and to meet the requirements for the next generation of semiconductor integrated circuits. On the other hand, it was found that vertical heterostructure transistors miss these performance targets by several orders of magnitude, both in terms of switching frequency and delay time, due to large intrinsic capacitances, and unavoidable current/capacitance tradeoffs.

In this chapter, we focus on the theoretical aspects of the planar technology of the graphene-based heterostructures. We will consider three types of these heterostructures: the single heterojunction, the quantum well, and the superlattice. Our analysis of the electronic properties of such heterostructures is based on the envelope wave function approach. In the first instance, this rather simple method gives an information about an energy spectrum of charge carriers. Then we can obtain a knowledge about optical and transport properties.

Here, we suggest to widely use the gap modifications of graphene in the planar heterostructures. We believe that the planar heterostructures made of gapless and gapped graphene are as prospective building blocks in future carbon-based nanoelectronics. The use of only gapless graphene reduces the diverse opportunities offered by bandgap engineering in gapped graphene.

2. Theoretical basis

2.1. The parity operator

Let us consider the parity operator in (3+1)QED [17]

$$\widehat{P} = i\gamma_4 \widehat{\Lambda}_{\mathbf{n}}. \tag{1}$$

Here, $i\gamma_4$ is the inversion operator and

$$\widehat{\Lambda}_{\mathbf{n}} = e^{-i\frac{\pi}{2}\Sigma\mathbf{n}} = -i\Sigma\mathbf{n}$$

is the operator of rotation by π about an $\mathbf{n}$ axis perpendicular to the graphene plane. In standard representation,

$$\Sigma = \begin{pmatrix} \sigma & 0 \\ 0 & \sigma \end{pmatrix},$$

where σ denotes Pauli matrices, and

$$\gamma_4 \equiv \beta = \begin{pmatrix} I & 0 \\ 0 & -I \end{pmatrix}$$

where I is the 2×2 unit matrix. It is clear that operator (1) is analogous to the parity operator $i\gamma_5\widehat{n}$ in QED, where $\widehat{n} = \boldsymbol{\gamma}\mathbf{n}$,

$$\boldsymbol{\gamma} = \begin{pmatrix} 0 & \sigma \\ -\sigma & 0 \end{pmatrix}, \quad \gamma_5 = \gamma_1\gamma_2\gamma_3\gamma_4 = i\begin{pmatrix} 0 & I \\ I & 0 \end{pmatrix}.$$

The eigen functions of this operator describe electron polarization states [18].

Charge carrier states in graphene can be described in terms of helicity defined as the eigenvalue of the operator $\widehat{h} = \sigma \cdot \mathbf{p}/(2|\mathbf{p}|)$. The projection of pseudospin on the direction of quasimomentum p indicates the valley in the Brillouin zone where electrons or holes belong (K or K' point in Fig. 2). Positive helicity corresponds to electrons and holes with wavevectors near the K and K' points, respectively; negative helicity corresponds to electrons and holes with wavevectors near the K' and K points, respectively [19].

Massless states with opposite helicities are decoupled [20]. In addition, charge carriers have chiral symmetry (helicity is conserved), and parity can be defined for both massless and massive carriers[1]. In other words, a higher symmetry of massless charge carriers implies the existence of an additional quantum number: helicity. Whereas parity distinguishes only between the valleys where carrier states belong ($\lambda = +1$ and -1 for states close to the K and K' points, respectively), helicity differs between a particle (electron) and an antiparticle (hole). However, chiral symmetry is broken for massive charge carriers. So, helicity is not a good quantum number any longer. Carrier states in a planar heterostructure combining gapless and gapped graphene should be characterized by parity.

Recall that the Dirac equation describing massless carriers in graphene in terms of 4×4 matrices is derived by assuming that they are spinless and have two valley degrees of freedom [10]. When analysis is restricted to charge carriers in one valley, the Dirac equation can be reduced to a 2×2 matrix representation by Weyl's equation for a massless fermion analogous to neutrino in two Euclidean dimensions [22]. The carrier energy spectrum with a pseudospin splitting in a planar heterostructure combining gapless and gapped graphene cannot be correctly analyzed in the 2×2 representation. For similar reasons, the representation of the Dirac algebra in terms of 2×2 matrices is not sufficient for describing the chiral symmetry breaking in (2+1)QED [23].

Using the two-dimensional 4×4 Dirac equation to describe charge carriers in a graphene-based nanostructure, we can study pseudospin effects following an approach to narrow-gap semiconductor heterostructures based on the Dirac model [24]. This makes methods developed for solving problems in the spintronics of narrow-gap semiconductor heterostructures applicable to graphene-based ones [25–33].

2.2. The equation for the envelope wavefunction

To describe some phenomena in graphene-based heterostructures, an equation containing a mass term should be written for the envelope wavefunction. A bandgap opening in the energy spectrum of graphene results from the lack of symmetry between the two triangular sublattices of its hexagonal lattice. The corresponding tight-binding Hamiltonian taking into account nearest-neighbor hopping has the form [34]

$$\widehat{H} = -t \sum_{\mathbf{B},i,\sigma} \left[a_\sigma^\dagger(\mathbf{B}+\mathbf{d}_i)b_\sigma(\mathbf{B}) + b_\sigma^\dagger(\mathbf{B})a_\sigma(\mathbf{B}+\mathbf{d}_i) \right]$$
$$+ \Delta \sum_{\mathbf{B},\sigma} \left[a_\sigma^\dagger(\mathbf{B}+\mathbf{d}_1)a_\sigma(\mathbf{B}+\mathbf{d}_1) - b_\sigma^\dagger(\mathbf{B})b_\sigma(\mathbf{B}) \right], \tag{2}$$

where $t \approx 2.8$ eV is the nearest-neighbor hopping energy; the sum runs over the position vectors $\mathbf{B}$ of all B sublattice atoms; $\sigma = \uparrow, \downarrow$ is the (pseudo)spin index; a_σ ($a_\sigma^\dagger$) and b_σ ($b_\sigma^\dagger$) are the annihilation (creation) operators of A and B sublattice electrons, respectively (see Fig. 1); and the parameter Δ quantifies the on-site energy difference between the two sublattices (setting $\Delta = 0$ restores the symmetry between sublattices so that graphene becomes gapless, whereas nonzero Δ equals the half-gap width in gapped graphene as shown below).

---

[1] Massless states can be characterized by two quantum numbers: helicity and sign of energy or helicity and eigenvalue of the operator $i\gamma_5$ [21]. Parity is analogous to the eigenvalue of $i\gamma_5$.
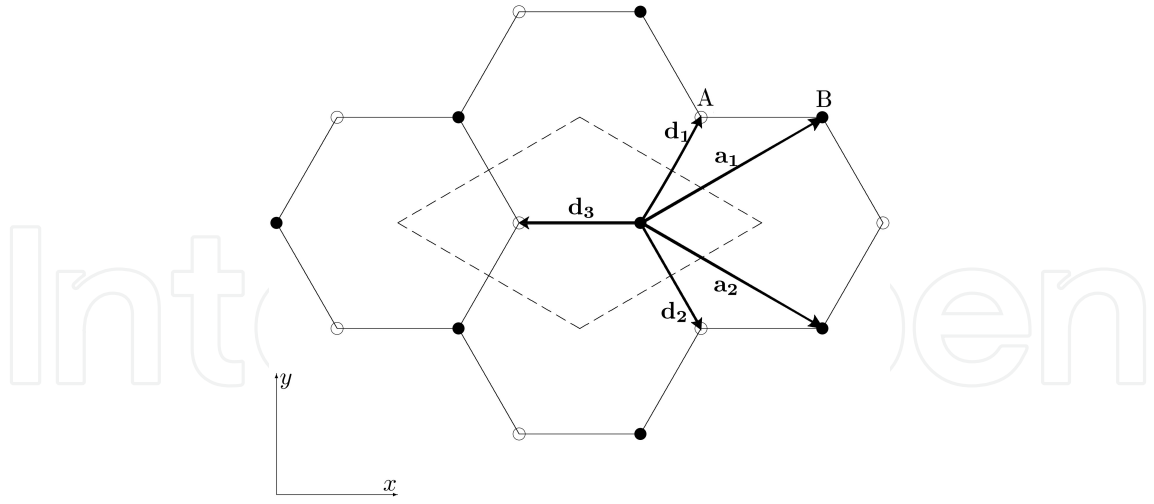
Figure 1. Part of hexagonal lattice, with highlighted vectors $\mathbf{d}_i$ from a B sublattice atom to the three nearest-neighbor A sublattice atoms.

Performing a Fourier transform, we change to the momentum representation

$$a_\sigma(\mathbf{A}) = \int_{\Omega_B} \frac{d^2k}{(2\pi)^2} a_\sigma(\mathbf{k}) e^{i\mathbf{k}\cdot\mathbf{A}}, \; b_\sigma(\mathbf{B}) = \int_{\Omega_B} \frac{d^2k}{(2\pi)^2} b_\sigma(\mathbf{k}) e^{i\mathbf{k}\cdot\mathbf{B}},$$

where Ω_B means integration over the first Brillouin zone (it is shown on Fig. 2).

Hamiltonian (2) is rewritten as

$$\widehat{H} = \sum_\sigma \int_{\Omega_B} \frac{d^2k}{(2\pi)^2} \left(a_\sigma^\dagger(\mathbf{k})\; b_\sigma^\dagger(\mathbf{k})\right) \begin{pmatrix} \Delta & -t\sum_i e^{-i\mathbf{k}\cdot\mathbf{d}_i} \\ -t\sum_i e^{i\mathbf{k}\cdot\mathbf{d}_i} & -\Delta \end{pmatrix} \begin{pmatrix} a_\sigma(\mathbf{k}) \\ b_\sigma(\mathbf{k}) \end{pmatrix}. \tag{3}$$

Conduction and valence band extrema lie at the corners of the first Brillouin zone. In the case of gapless graphene, they touch each other and there are the cone-like energy surfaces at the K and K' points (see Fig. 3). We use Hamiltonian (3) expanded around the K point with quasimomentum $\mathbf{q}_1 = \left(\frac{2\pi}{3a}, \frac{2\pi}{3\sqrt{3}a}\right)$ or around the K' point with $\mathbf{q}_2 = \left(\frac{2\pi}{3a}, -\frac{2\pi}{3\sqrt{3}a}\right)$

$$\widehat{H} = \sum_\sigma \int \frac{d^2k}{(2\pi)^2} \widehat{\Psi}_\sigma^\dagger(\mathbf{k}) \widehat{\mathcal{H}} \widehat{\Psi}_\sigma(\mathbf{k}).$$

where integration is performed over small neighbor-hoods of the K and K' points. Near the corners, the Hamiltonian reduces to

$$\widehat{\mathcal{H}} = \begin{pmatrix} v_F \boldsymbol{\sigma}\cdot\mathbf{k} + \Delta\sigma_z & 0 \\ 0 & v_F \boldsymbol{\sigma}^*\cdot\mathbf{k} + \Delta\sigma_z \end{pmatrix}, \tag{4}$$
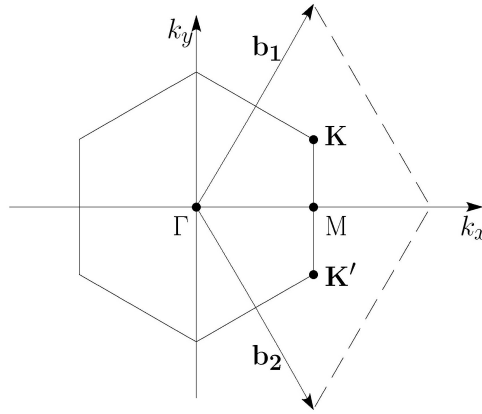
Figure 2. The first Brillouin zone of graphene, with linear energy spectrum at the corners (Dirac points). The reciprocal lattice vectors $\mathbf{b}_1 = (2\pi/3a, 2\pi/\sqrt{3}a)$ and $\mathbf{b}_2 = (2\pi/3a, -2\pi/\sqrt{3}a)$, where $a=1.42$ Å is the lattice spacing, combined with the dashed lines equivalently represent the first Brillouin zone as a rhombus.

where $v_F = \frac{3}{2}at$ is the carrier Fermi velocity, $\boldsymbol{\sigma} = (\sigma_x, \sigma_y)$ and $\boldsymbol{\sigma}^* = (\sigma_x, -\sigma_y)$ are Pauli matrices in the sublattice space, and $\widehat{\Psi}_\sigma(\mathbf{k})$ is the bispinor defined as

$$\widehat{\Psi}_\sigma(\mathbf{k}) = \begin{pmatrix} \widehat{\Psi}_\sigma^{(1)}(\mathbf{k}) \\ \widehat{\Psi}_\sigma^{(2)}(\mathbf{k}) \end{pmatrix},$$

in terms of

$$\widehat{\Psi}_\sigma^{(1,2)}(\mathbf{k}) = \exp\left(\frac{5\pi i}{12}\sigma_z\right) \sigma_z \begin{pmatrix} a_\sigma(\mathbf{q}_{1,2} + \mathbf{k}) \\ b_\sigma(\mathbf{q}_{1,2} + \mathbf{k}) \end{pmatrix}.$$

We write an equation for the envelope wavefunction in a planar heterostructure:

$$\left[v_{Fj} \left(\tau_0 \otimes \sigma_x \widehat{p}_x + \tau_z \otimes \sigma_y \widehat{p}_y \right) + \tau_0 \otimes \sigma_z \Delta_j + \tau_0 \otimes \sigma_0 \left(V_j - E \right) \right] \Psi(x,y) = 0. \tag{5}$$

Here, $\Delta_j = E_{gj}/2$ $(j = 1, 2, \ldots)$ denotes half-width of bandgap; the respective work functions V_j depend on the mid-gap energies relative to the Dirac points for the corresponding materials; the 2×2 unit matrix σ_0 acts in the sublattice space; the 2×2 unit matrix τ_0 and the matrix τ_z defined similar to the Pauli matrix σ_z act in the valley space; $\otimes$ is the Kronecker product symbol; and $\widehat{p}_x = -i\partial_x$ and $\widehat{p}_y = -i\hbar\partial_y$ are the momentum operator components. Assuming that the carrier Fermi velocities may differ between the regions, we denote those for gapped jth regions by v_{Fj} for both gapless graphene and its gapped modifications.

Charge carriers move freely along the y axis:

$$\Psi(x,y) = \Psi(x)e^{ik_y y}.$$

The wavefunction $\Psi(x)$ is a bispinor:

$$\Psi(x) = \begin{pmatrix} \psi_K(x) \\ \psi_{K'}(x) \end{pmatrix},$$

where the spinors $\psi_K(x)$ and $\psi_{K'}(x)$ represent charge carriers in the K and K' valleys, respectively:

$$\psi_K(x) = \begin{pmatrix} \psi_{KA}(x) \\ \psi_{KB}(x) \end{pmatrix}, \quad \psi_{K'}(x) = \begin{pmatrix} \psi_{K'A}(x) \\ \psi_{K'B}(x) \end{pmatrix}.$$

In the present context, the parity operator is expressed as follows:

$$\widehat{P} = \tau_z \otimes \sigma_0. \tag{6}$$

Equation (5) is solved here in the parity basis. The eigenfunctions $\Psi_\lambda(x)$ of parity operator (6) are defined as follows:

$$\widehat{P}\Psi_\lambda(x) = \lambda\Psi_\lambda(x),$$

$$\Psi_{+1}(x) = \begin{pmatrix} \psi_{+1,K}(x) \\ 0 \end{pmatrix},$$

$$\Psi_{-1}(x) = \begin{pmatrix} 0 \\ \psi_{-1,K'}(x) \end{pmatrix}. \tag{7}$$
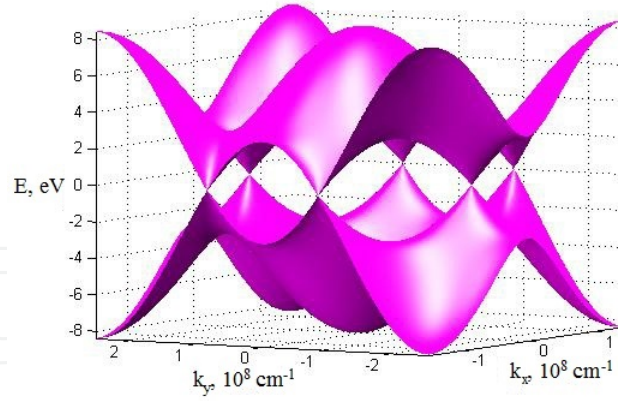
Rewriting Eq. (5) as the 2×2 matrix equations

$$\left(-iv_{Fj}\sigma_x\partial_x + v_{Fj}k_y\sigma_y + \lambda\Delta_j\sigma_z + V_j \right)\psi_{\lambda K}(x) = E_\lambda\psi_{\lambda K}(x), \tag{8}$$

$$\left(-iv_{Fj}\sigma_x\partial_x - v_{Fj}k_y\sigma_y - \lambda\Delta_j\sigma_z + V_j \right)\psi_{\lambda K'}(x) = E_\lambda\psi_{\lambda K'}(x). \tag{9}$$

We see that setting $\Delta_j = 0$ and $V_j = 0$ brings us back to the spinor wavefunctions describing chiral states near the K or K' point, where the operator $\widehat{h}$ can be defined. However, chiral symmetry is broken when $\Delta \neq 0$ (see previous section). Defining parity λ as the eigenvalue of operator (6), we find that it indicates the valley where charge carriers belong: by virtue of (7), $\lambda = +1$ for the states near the K point described by Eq. (8) and $\lambda = -1$ for the states near the K' point described by Eq. (9).

In both gapped and gapless graphene, the valleys transform into each other under time reversal. This is indicated by the opposite signs of the terms proportional to k_y in Eqs. (8) and (9), since $k_y \to -k_y$ under time reversal. It can be shown directly by using the time reversal operator $\mathcal{T}$ in explicit form that $\lambda \to -\lambda$ under $\mathcal{T}$. Indeed, if k_y is parallel to the line $K - M - K'$ (see Fig. 2) and its origin is set at M, then $K \to K'$ and $K' \to K$ under $\mathcal{T}$.

Figure 3. The energy surface for gapless graphene.

Equations (8) and (9) are equivalently rewritten as the 2×2 matrix equation

$$\left(-iv_{Fj}\sigma_x\partial_x + \lambda v_{Fj}k_y\sigma_y + \Delta_j\sigma_z + V_j\right)\psi_\lambda(x) = E_\lambda\psi_\lambda(x). \tag{10}$$

Hereinafter, valley indices K and K' are omitted as unnecessary since λ specifies the valley where charge carriers belong.

2.3. The boundary conditions

Now, let us discuss the boundary conditions at the interfaces between different graphene materials. At the outset, we note that they are easier to formulate than those used at the graphene–free-space interface in models of edge states [6, 35]. To derive boundary conditions in the present model, we must find a relation between $\psi_\lambda(l)$ and $\psi_\lambda(-l)$ as $l \to 0$ in the neighbor-hood of x = 0, where l goes down to an atomic scale (condition at x = d is derived similarly). Multiplying Eq. (10) by $\psi^\dagger(x)$ on the left, we integrate it over $[-l, l]$. Since a is small, we neglect all terms except those containing a derivative with respect to x to obtain[2]

$$\psi_\lambda^{(-)\dagger}(-l)v_F^{(-)}\psi_\lambda^{(-)}(-l) = \psi_\lambda^{(+)\dagger}(l)v_F^{(+)}\psi_\lambda^{(+)}(l),$$

where $\psi_\lambda^{(-)}$ and $\psi_\lambda^{(+)}$ are defined on the left- and right-hand sides of the boundary (at $x < 0$ and $x > 0$, respectively). Representing these functions as

$$\psi_\lambda^{(\pm)} = \left|\psi_\lambda^{(\pm)}\right|\exp\left(i\varphi^{(\pm)}\right),$$

we rewrite the equality above as

$$\sqrt{v_F^{(-)}}\left|\psi_\lambda^{(-)\dagger}(-l)\right| = \sqrt{v_F^{(+)}}\left|\psi_\lambda^{(+)\dagger}(l)\right|.$$

---

[2] From the given equality, we have the continuity of the current component normal to the interface in the heterostructure plane. It is necessary condition.

To formulate the boundary condition in final form, we assume that the difference between phases of $\psi_\lambda^{(-)}$ and $\psi_\lambda^{(+)}$ near the interface is a multiple of 2π:

$$\varphi^{(+)} = \varphi^{(-)} + 2\pi n, \quad n \in \mathbb{Z}.$$

As l goes to zero, we obtain the following wavefunction-matching condition [26, 27]

$$\sqrt{v_F^{(-)}} \psi_\lambda^{(-)} = \sqrt{v_F^{(+)}} \psi_\lambda^{(+)}, \tag{11}$$

where minus and plus signs refer to the materials on the left- and right-hand sides of the boundary, respectively.
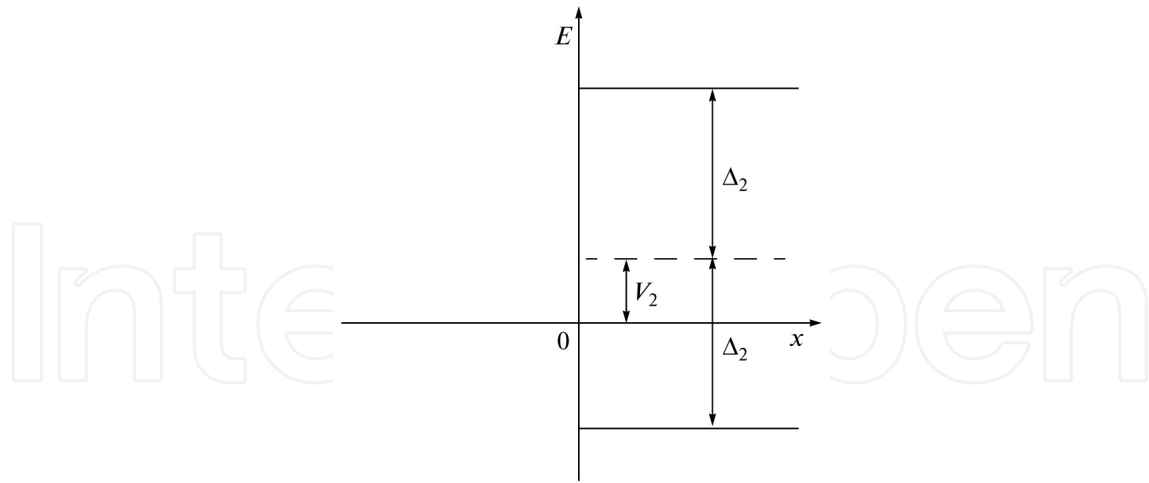
3. Graphene heterojunctions

We consider a planar heterojunction composed of graphene and a gap modification of graphene [36]. When we say a gap modification of graphene we imply a graphene with an energy gap in the Dirac spectrum of charge carriers. There are several gap modifications of graphene.

First, the energy gap can open because graphene sheets are located not on SiO_2 substrate but on some other material, for example, h-BN, when two triangular sublattices of graphene become nonequivalent and a gap modification of graphene is formed with an energy gap of 53 meV [37]. Second, the energy gap opens in the epitaxially grown graphene on the SiC substrate [38], which is equal to 0.26 eV according to experimental results obtained by angular-resolved photoemission spectroscopy [39]. Third, recently another modification of graphene, i.e., graphane, was synthesized by hydrogenation [40], which has a direct energy gap of 5.4 eV at the Γ point according to the calculations [41]. In the first two cases, a graphene film deposited on inhomogeneous SiO_2–h-BN or SiO_2–SiC substrates can be used (Fig. 4a shows the case with h-BN). In the third case, an inhomogeneously hydrogenated graphene is used (a part of the graphene sample is left without hydrogenation, Fig. 4b).

We assume that the energy gap in the gap modifications of graphene opens at K and K' points of the first Brillouin zone, which correspond to the Dirac points of gapless graphene.
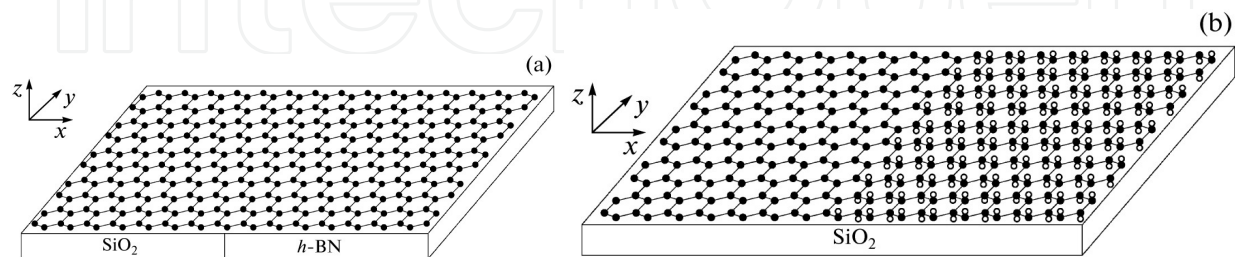
Figure 4. Two variants of the system in question: **(a)** graphene layer on the substrate composed of h-BN and SiO_2 and **(b)** nonuniformly hydrogenated graphene on the SiO_2 substrate. Open circles are hydrogen atoms, which are located so that they are bound to carbon atoms of one sublattice on one side of graphene sheet and to carbon atoms of the other sublattice on the other side.

Figure 5. Graphene heterojunction under consideration.

Let us assume that the x axis is directed along the plane of the heterojunction perpendicular to the boundary between graphene and its gap modification and the y axis is directed along the boundary. The z axis is directed perpendicular to the plane of the heterojunction. The half-plane $x < 0$ is occupied by the gap-less graphene and the half-plane $x > 0$ belongs to the gap modification of graphene. So, the line $x = 0$ is the boundary under consideration.

In this case, the parameters in Eq. (5) with $j = 1$ are related to the gapless graphene and the parameters with $j = 2$ are related to the gap modification of the graphene: v_{F1} and v_{F2} are the Fermi velocities (in the general case, $v_{F2} \neq v_{F1}$, and $v_{F1} \approx 10^8$ cm/s); $\Delta_1 = 0$ and $\Delta_2 \neq 0$ are the half-widths of the energy gaps; V_1 and V_2 are the work functions (V_2 determines position of the middle of the energy gap for the gap modification of the graphene with respect to the Dirac points of the gapless graphene, and $V_1 = 0$ is chosen for the origin, see Fig. 5).

In order to avoid spontaneous generation of electron-hole pairs, we assume that the heterojunction in question is a junction of the first kind, i.e., the Dirac points of gapless graphene are located inside the energy gap of its gap modification. This limits value of the work function $|V_2| < \Delta_2$.

Equation (5) is solved within the class of wave eigenfunctions $\Psi_\lambda(x)$ of the parity operator (6) for two areas on both sides from the boundary.

Equation (5) can be easily represented as two 2×2 matrix equations

$$\left(-iv_{Fj}\sigma_x\frac{d}{dx} + v_{Fj}k_y\sigma_y + \lambda\Delta_j\sigma_z + V_j\right)\Psi_{\lambda K}(x) = E_\lambda\Psi_{\lambda K}(x), \tag{12}$$

$$\left(-iv_{Fj}\sigma_x\frac{d}{dx} - v_{Fj}k_y\sigma_y - \lambda\Delta_j\sigma_z + V_j\right)\Psi_{\lambda K'}(x) = E_\lambda\Psi_{\lambda K'}(x). \tag{13}$$

In this case, we have $\lambda = +1$ in Eq. (12) and $\lambda = -1$ in Eq. (13).

The solution to Eq. (12) for boundary states has the form

$$\Psi_{\lambda K}(x) = \begin{cases} C\binom{1}{a}\exp(\kappa_1 x), & x < 0, \\ C\binom{b}{qb}\exp(-\kappa_2 x), & x > 0, \end{cases} \quad (14)$$

where

$$a = i\frac{v_{F1}(k_y - \kappa_1)}{E_\lambda}, \quad q = i\frac{v_{F2}(k_y + \kappa_2)}{E_\lambda - V_2 + \lambda\Delta_2},$$

C is the normalization factor, $b = \sqrt{\frac{v_{F1}}{v_{F2}}}$ is the constant obtained when matching solutions for $x < 0$ and $x > 0$ at the line $x = 0$ under condition (11),

$$E_\lambda = \pm v_{F1}\sqrt{k_y^2 - \kappa_1^2}, \quad (15)$$

from which it follows that the necessary condition for the existence of the boundary states is given by inequality

$$\kappa_1 < |k_y|. \quad (16)$$

Equation (15) can be rewritten as

$$\kappa_1 = \sqrt{k_y^2 - E_\lambda^2/v_{F1}^2},$$

Therefore, the following inequality should also be valid

$$|E_\lambda| < v_{F1}|k_y|. \quad (17)$$

Expression for κ_2 is represented in the form

$$\kappa_2 = \frac{1}{v_{F2}}\sqrt{\Delta_2^2 - (E_\lambda - V_2)^2 + v_{F2}^2 k_y^2}.$$

Moreover, the matching leads to the inequality

$$\frac{v_{F1}(k_y - \kappa_1)}{E_\lambda} = \frac{v_{F2}(k_y + \kappa_2)}{E_\lambda - V_2 + \lambda\Delta_2}. \quad (18)$$

The solution to Eq. (13) is produced from Eq. (14) by the following substitutions in factors a and q: $k_y \to -k_y$ and $\lambda \to -\lambda$.

Let us discuss separately the case of zero mode $E_\lambda = 0$. Components of the envelope wave function in $x < 0$ region (gapless graphene) $\Psi_{\lambda K} = \binom{a_1}{a_2} \exp(\kappa_1 x)$ satisfy equations:

$$(\kappa_1 - k_y)a_1 = 0,$$
$$(\kappa_1 + k_y)a_2 = 0,$$

i.e., either $\kappa_1 = k_y$ ($k_y > 0$) and $a_2 = 0$, or $\kappa_1 = -k_y$ ($k_y < 0$) and $a_1 = 0$. Then it follows from the matching condition (11) that both components of the envelope wave function are zero in $x > 0$ region ($b = 0$); therefore, we have $a_1 = 0$ and $a_2 = 0$, i.e., $\Psi_{\lambda K}(x) \equiv 0$. Thus, there is no zero mode for the boundary states in question.

The following equations are easily obtained from Eq. (18):

$$\kappa_1 \kappa_2 = \frac{E_\lambda(E_\lambda - V_2)}{v_{F1} v_{F2}} - k_y^2, \qquad (19)$$

$$\lambda \Delta_2 E_\lambda = v_{F1} v_{F2} k_y (\kappa_1 + \kappa_2). \qquad (20)$$

The two latter equations are valid for either value of λ (for both valleys), because they are invariant in respect to simultaneous substitutions $k_y \to -k_y$ and $\lambda \to -\lambda$.

Since $\kappa_1 > 0$ and $\kappa_2 > 0$, right-hand side of Eq. (19) should be positive. Let us denote by $\varepsilon_0(k_y)$ such value of E_λ that the right-hand side of Eq. (19) turns zero,

$$\varepsilon_0(k_y) = \frac{V_2}{2} \pm \sqrt{\frac{V_2^2}{4} + v_{F1} v_{F2} k_y^2}, \qquad (21)$$

where "+" corresponds to electrons and "−" to holes. Then, the condition $\kappa_1 \kappa_2 > 0$ is equivalent to the inequality

$$|E_\lambda| > |\varepsilon_0(k_y)|. \qquad (22)$$

It follows from Eq. (20) that inequality $\lambda k_y > 0$ holds for electron boundary states ($E_\lambda > 0$), and $\lambda k_y < 0$ holds for hole boundary states ($E_\lambda < 0$). The boundary states are not degenerate in parity. That means that there is no Kramers degeneracy of energy spectrum for them. This is also true for boundary states in a planar quantum well based on graphene nanoribbon [42] and for boundary states localized on zigzag edges of gapless graphene [43]. Since parity determines charge carrier attribution to one of two valleys, the property mentioned above means also that there is a "valley polarization" of boundary states: electrons that move along the heterojunction boundary with $k_y > 0$ are located near K point and electrons with $k_y < 0$ are near K' point and vise versa in case of holes. Because of that, current that flows along the heterojunction boundary would be "valley-polarized" [36].

By squaring Eq. (20) we get a quadratic equation, solution of which produces dependence of energy on k_y:

$$E_\lambda(k_y) = \frac{v_{F1}v_{F-}k_y^2 V_2 + \lambda v_{F1}k_y\Delta_2\sqrt{\Delta_2^2 + v_{F-}^2 k_y^2 - V_2^2}}{\Delta_2^2 + v_{F-}^2 k_y^2}, \tag{23}$$

where $v_{F-} = v_{F1} - v_{F2}$. Equation (23) takes into account that sign of λk_y determines type of charge carriers in the boundary states.

It is easy to verify that inequality (17) is always true if the energy is given by Eq. (23). Therefore, inequality (16) also holds.

Now, it is simple to analyze inequality (22). Let us introduce the following notation:

$$k_{y1} = \frac{|V_2|}{|v_{F-}|},$$

$$k_{y2,3} = \sqrt{\frac{v_{F2}V_2^2 + 2v_{F-}\Delta_2^2 \mp |V_2|\sqrt{v_{F2}^2 V_2^2 + 4v_{F1}v_{F-}\Delta_2^2}}{2v_{F2}v_{F-}^2}}.$$

Under the condition

$$v_{F1} < v_{F2} < 2v_{F1}, \quad \frac{2}{v_{F2}}\sqrt{v_{F1}|v_{F-}|}\Delta_2 < |V_2| < \Delta_2, \tag{24}$$

the boundary states exist in the ranges[3]

$$0 < |k_y| < k_{y2}, \quad k_{y3} < |k_y| < k_{y1}$$

either for electrons, if $V_2 < 0$, or for holes, if $V_2 > 0$.

Under condition

$$v_{F1} < v_{F2} < 2v_{F1}, \quad |V_2| < \frac{2}{v_{F2}}\sqrt{v_{F1}|v_{F-}|}\Delta_2 \tag{25}$$

the boundary states exist in the range

$$0 < |k_y| < k_{y1}$$

either for electrons, if $V_2 < 0$, or for holes, if $V_2 > 0$.

Under the condition

$$v_{F1} > v_{F2}, \quad 0 < V_2 < \Delta_2 \tag{26}$$

---

[3] Here and below, we exclude the point $k_y = 0$, because it corresponds to $E_\lambda = 0$.

the electron boundary states exist in the range

$$k_{y3} < |k_y| < k_{y1},$$

and the hole boundary states exist in the range

$$0 < |k_y| < k_{y2}.$$

Under condition

$$v_{F1} > v_{F2}, \quad -\Delta_2 < V_2 < 0$$

the electron boundary states exist in the range

$$0 < |k_y| < k_{y2},$$

and the hole boundary states exist in the range

$$k_{y3} < |k_y| < k_{y1}.$$

Let us consider three special cases.

(1) Under condition $V_2 = 0$ and $v_{F-} \neq 0$, the boundary states exist for both electrons and holes in the following range if $v_{F1} > v_{F2}$
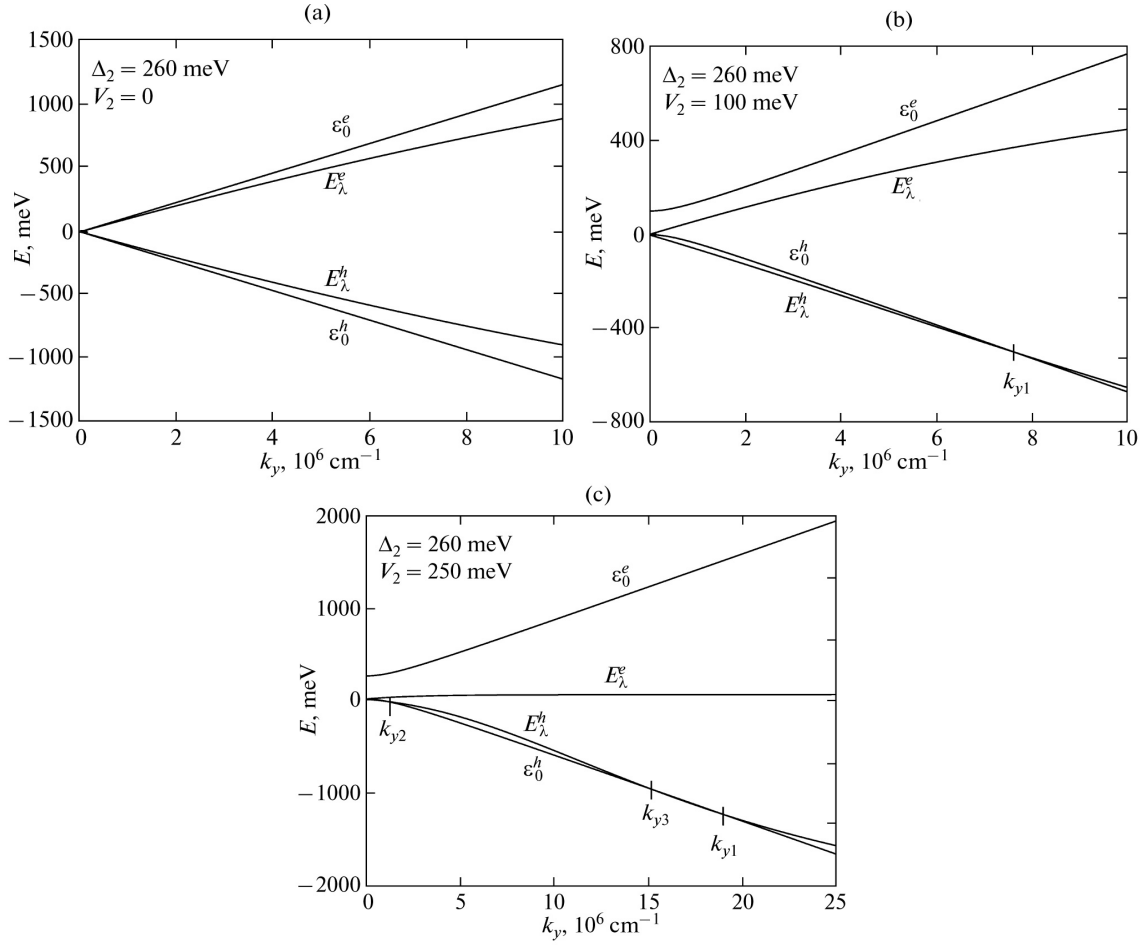
$$0 < |k_y| < \frac{\Delta_2}{\sqrt{v_{F1}v_{F-}}}. \tag{27}$$

(2) Under condition $v_{F1} = v_{F2}$, $0 < |V_2| < \Delta_2$ the boundary states exist in the range

$$0 < |k_y| < \frac{\Delta_2\sqrt{\Delta_2^2 - V_2^2}}{v_{F2}|V_2|} \tag{28}$$

either for electrons, if $V_2 < 0$, or for holes, if $V_2 > 0$.

(3) Under condition $v_{F1} = v_{F2}$, $V_2 = 0$, the boundary states are absent both for electrons and holes, because $|E_\lambda(k_y)| = |\varepsilon_0(k_y)|$, which is in contradiction with inequality (16).

Figure 6. Dispersion curves $E_\lambda^{e,h}(k_y)$ and $\varepsilon_0^{e,h}(k_y)$: **(a)** there are no boundary states for electrons and holes at $V_2 = 0$, **(b)** there are only hole boundary states in the range $0 < |k_y| < k_{y1}$ at $V_2 = 100$ meV, and **(c)** there are only hole boundary states in the ranges $0 < |k_y| < k_{y2}$ and $k_{y3} < |k_y| < k_{y1}$ at $V_2 = 250$ meV.

Fig. 6 shows dispersion curves $E_\lambda^{e,h}(k_y)$ and $\varepsilon_0^{e,h}(k_y)$ for the electron and hole boundary states for three values of V_2 in the model of graphene-based heterojunction with $\Delta_2 = 260$ meV and $v_{F2} = 1.2 \times 10^8$ cm/s for gap modification of graphene.

Our results remain in essence the same if instead of a sharp heterojunction we consider a smooth heterojunction. Indeed, let $v_F(x)$ and $\Delta(x)$ vary smoothly from their values for gapless graphene to their values in gap modification of graphene over a strip with the width $d \lesssim \kappa_{1,2}^{-1}$. Then change in energy of the boundary states is $|\delta E_\lambda(k_y)| \lesssim 1$ meV. Such insignificant variation in energy of the boundary states produces no noticeable qualitative changes. A similar result has been obtained for boundary states in heterojunctions of narrow-gap semiconductors with intercrossing dispersion curves in [44].

To conclude, we would like to point out that the new type of boundary states in graphene heterojunctions can be studied in experiment by tunnel spectroscopy of angular-resolved photoemission spectroscopy similar to how it have been done for boundary states in gapless graphene [45–47].

4. Graphene quantum well

4.1. General consideration

In this study, we examine a planar quantum well (QW) made of a graphene nanoribbon whose edges are in contact with gapped graphene sheets.

A bandgap opening in graphene can be induced by several methods. First, graphene can be deposited on h-BN substrate instead of a silicon-oxide one. This makes its two triangular sublattices nonequivalent, inducing in a bandgap of 53 meV [37]. Second, epitaxial graphene grown on a silicon-carbide substrate also has a nonzero bandgap [38]. According to angle-resolved photoemission data, a bandgap of 0.26 eV is produced by this method [39]. Third, a hydrogenated derivative of graphene synthesized recently, graphane [40], has been predicted to have a direct bandgap of 5.4 eV at the Γ point [41]. Fourth, *ab initio* calculations have shown that CrO_3 adsorption on graphene induces a gap of 0.12 eV [48]. In the first two methods, a heterogeneous substrate can be used, such as an h-BN — SiO_2 nanoribbon — h-BN or SiC — SiO_2 nanoribbon — SiC one (Fig. 7a depicts a substrate with h-BN). The last two methods produce a graphene sheet containing a nanoribbon without hydrogenation (as the nonhydrogenated one in Fig. 7b) or a graphene strip without adsorbed CrO_3 molecules, respectively. Furthermore, the bandgap can be varied by using partially hydrogenated graphene (where some carbon atoms are not bonded to hydrogen atoms). Combinations of these methods can also be employed. Extensive experimental studies of graphene on substrates made of various materials, including rare-earth metals, have been reported recently [49–51]. It may be possible to open a bandgap via adsorption of other molecules on graphene or by using other materials as substrates. The use of gapped graphene to create potential barriers opens up additional possibilities for bandgap engineering in carbon-based materials [52].

In the case of QW, in Eq. (10) $\Delta_j = E_{gj}/2$ ($j = 1, 2, 3$) denotes half-width of bandgap ($\Delta_1 \neq 0$ and $\Delta_3 \neq 0$ in regions *1* and *3*, whereas $\Delta_2 = 0$ region *2*); the respective work functions V_1 and V_3 of regions *1* and *3* depend on the mid-gap energies relative to the Dirac points for the corresponding materials (we set $V_2 = 0$ to be specific, see Fig. 8).

The solution to Eq. (10) is expressed as follows.
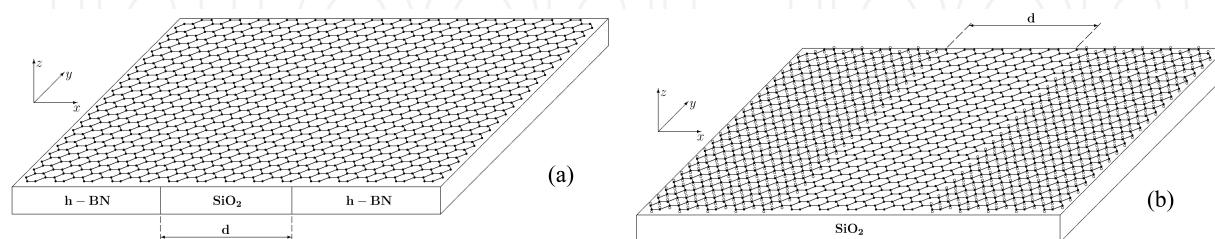
Figure 7. Two configurations of the system under study: **(a)** graphene sheet on a substrate consisting of a SiO_2 nanoribbon of width d inserted between h–BN nanoribbons; **(b)** a graphene sheet on a SiO_2 substrate containing a nonhydrogenated nanoribbon of width *d*, where open and closed circles are hydrogen atoms bonded to carbon atoms in different sublattices on opposite sides of the sheet, respectively.
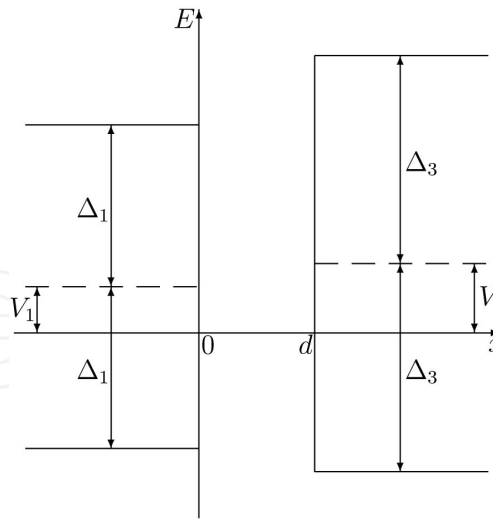
Figure 8. An energy scheme of QW under analysis.

1. At $x < 0$,

$$\psi_\lambda(x) = C \begin{pmatrix} 1 \\ q_1 \end{pmatrix} e^{k_1 x}, \tag{29}$$

where

$$q_1 = -i \frac{v_{F1}(k_1 - \lambda k_y)}{E_\lambda - V_1 + \Delta_1},$$

$$v_{F1} k_1 = \sqrt{\Delta_1^2 - (E_\lambda - V_1)^2 + v_{F1}^2 k_y^2}.$$

2. At $0 < x < d$,

$$\psi_\lambda(x) = C \begin{pmatrix} \kappa^* \\ q_2 \kappa^* \end{pmatrix} e^{ik_2 x} + C \begin{pmatrix} \kappa \\ -q_2 \kappa \end{pmatrix} e^{-ik_2 x}, \tag{30}$$

where

$$\kappa = \frac{1}{2} \sqrt{\frac{v_{F1}}{v_{F2}}} \left[1 + i \left(\frac{\lambda k_y}{k_2} + \frac{v_{F1}(k_1 - \lambda k_y)E_\lambda}{v_{F2} k_2 (E_\lambda - V_1 + \Delta_1)} \right) \right],$$

$$q_2 = \frac{v_{F2}(k_2 + i\lambda k_y)}{E_\lambda}, \qquad E_\lambda = \pm v_{F2} \sqrt{k_2^2 + k_y^2},$$

with plus and minus corresponding to electrons and holes, respectively.

3. At $x > d$,

$$\psi_\lambda(x) = C \begin{pmatrix} \zeta \\ q_3 \zeta \end{pmatrix} e^{-k_3(x-d)}, \tag{31}$$

where

$$\zeta = \sqrt{\frac{v_{F1}}{v_{F3}}} \left[\cos(k_2 d) + \left(\frac{\lambda k_y}{k_2} + \frac{v_{F1}(k_1 - \lambda k_y)E_\lambda}{v_{F2}k_2(E_\lambda - V_1 + \Delta_1)} \right) \sin(k_2 d) \right],$$

$$q_3 = i \frac{v_{F3}(k_3 + \lambda k_y)}{E_\lambda - V_3 + \Delta_3},$$

$$v_{F3}k_3 = \sqrt{\Delta_3^2 - (E_\lambda - V_3)^2 + v_{F2}^2 k_y^2}.$$

The constant C is found by using the normalization condition for wavefunctions (29)—(31),

$$\int_{-\infty}^{\infty} \Psi_\lambda^\dagger(x)\Psi_\lambda(x)dx = 1.$$

The carrier energy spectrum is determined by the dispersion relation

$$\tan(k_2 d) = v_{F2}k_2 f(\lambda k_y; k_1, k_3, E_\lambda), \qquad (32)$$

where

$$f(\lambda k_y; k_1, k_3, E_\lambda) = \left[v_{F1}(k_1 - \lambda k_y)(E_\lambda - V_3 + \Delta_3) + v_{F3}(k_3 + \lambda k_y)(E_\lambda - V_1 + \Delta_1) \right]$$
$$\times \left[E_\lambda(E_\lambda - V_1 + \Delta_1)(E_\lambda - V_3 + \Delta_3) - v_{F2}v_{F3}\lambda k_y(k_3 + \lambda k_y)(E_\lambda - V_1 + \Delta_1) \right.$$
$$\left. + v_{F1}v_{F2}\lambda k_y(k_1 - \lambda k_y)(E_\lambda - V_3 + \Delta_3) - v_{F1}v_{F3}(k_1 - \lambda k_y)(k_3 + \lambda k_y)E_\lambda \right]^{-1}$$

is a function of k_2 as well. Equation (32) must be solved for k_2, and then the energy E_λ is found.

In the case of an asymmetric QW, the dependence of (32) on λ gives rise to pseudospin splitting as the extrema of the dispersion curves shift away from Brillouin-zone corners. The dispersion relation predicts that $E_\lambda(k_y) \neq E_{-\lambda}(k_y)$, and an energy splitting appears near the conduction-band bottom at $k_y = k_{ye}^*$:

$$\delta E_s^e = |E_{-1}^e(k_{ye}^*) - E_{+1}^e(k_{ye}^*)|.$$

A similar energy splitting appears near the valence-band top at $k_y = k_{ye}^*$:

$$\delta E_s^h = |E_{-1}^h(k_{yh}^*) - E_{+1}^h(k_{yh}^*)|$$

Thus, a graphene nanoribbon becomes an indirect band-gap semiconductor analogous to silicon and germanium, where an electron-hole plasma can exist [53]. In the case of a symmetric QW ($\Delta_1 = \Delta_3$, $V_1 = V_3$, $v_{F1} = v_{F3}$) band structure is invariant under parity and there is no pseudospin splitting [42].
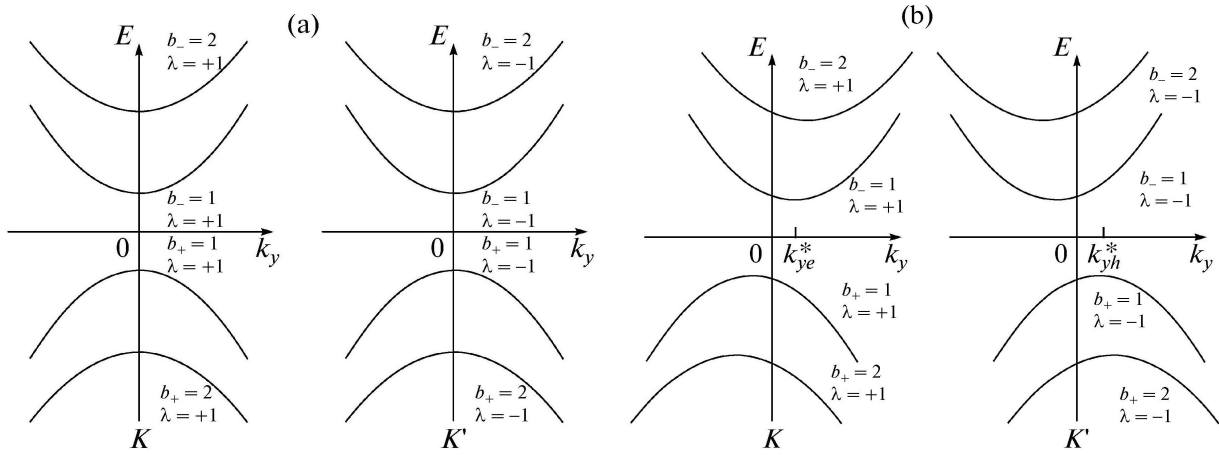
Figure 9. Energy spectra: **(a)** symmetric QW (no pseudospin splitting), with matching branches for $\lambda = +1$ and $\lambda = -1$ ($E_\lambda(k_y) = E_{-\lambda}(k_y) = E_\lambda(-k_y)$); **(b)** asymmetric QW, with pseudospin splitting manifested by the "spread-out" in quasimomentum between the extrema at k_{ye}^* for electrons, shown for $b_- = 1$, and at k_{yh}^* for holes, shown for $b_+ = 1$ ($E_\lambda(k_y) \neq E_{-\lambda}(k_y)$).

4.2. Size quantization

Solving Eq. (32), we determine the size-quantized energies

$$E_{\lambda b_\mp}(k_y) = \pm v_{F2}\sqrt{k_{2b_\mp}^2(\lambda k_y) + k_y^2},$$

where $b_\mp = 1, 2, \ldots$ labels electron ($-$) and hole ($+$) branches, respectively. The size-quantized energy spectra for symmetric and asymmetric QW are shown schematically in Fig. 9.

We now determine the carrier effective masses arising because of size quantization in the graphene nanoribbon in a planar heterostructure. Note that the effective masses are invariant under parity regardless of pseudospin splitting. Hereinafter, we omit indices $b_\mp$, restricting ourselves to a particular branch of the electron spectrum and a particular branch of the hole spectrum.

We write the dispersion law for electrons near an extremum at λk_{ye}^* as

$$E_\lambda^e \approx E_0^e + \frac{1}{2m_e^*}\left(k_y - \lambda k_{ye}^*\right)^2,$$

$$m_e^* = \frac{1}{v_{F2}}\frac{\sqrt{k_{20e}^2 + k_{ye}^{*2}}}{1 + k_{20e}^{'2} + k_{20e}k_{20e}^{''}},$$

(33)

where the respective values k_{20e}, k_{20e}', k_{20e}'' of $k_{2e}(k_y)$ and its first and second derivatives at $k_y = \lambda k_{ye}^*$ are independent of λ; $E_0^e = v_{F2}\sqrt{k_{20e}^2 + k_{ye}^{*2}}$ is the energy at the extremum.
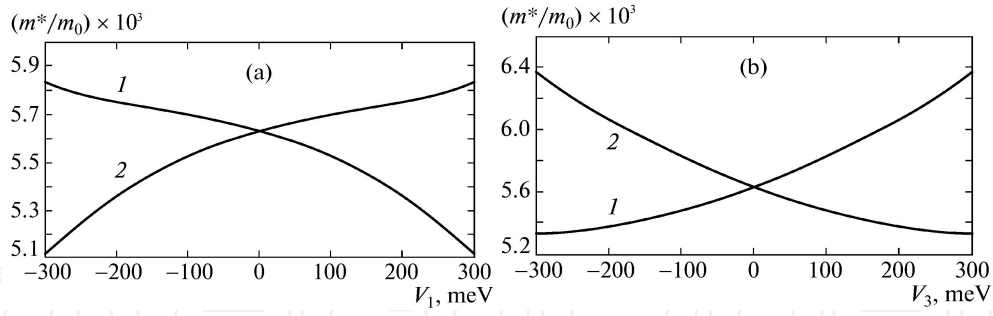
Figure 10. Electron (curves *1*) and hole (curves *2*) effective masses in the graphene nanoribbon (in units of free-electron mass m_0) as functions of V_1 for $V_3 = 0$ **(a)** and as functions of V_3 for $V_1 = 0$ **(b)**.

Analogous expressions are obtained for hole energies:

$$E_\lambda^h \approx E_0^h + \frac{1}{2m_h^*}\left(k_y - \lambda k_{yh}^*\right)^2,$$

$$m_h^* = \frac{1}{v_{F2}}\frac{\sqrt{k_{20h}^2 + k_{ye}^{*2}}}{1 + k_{20h}^{\prime 2} + k_{20e}k_{20h}^{\prime\prime}}, \tag{34}$$

where the respective values k_{20h}, k_{20h}', k_{20h}'' of $k_{2h}(k_y)$ and its first and second derivatives at $k_y = -\lambda k_{yh}^*$; $E_0^h = -v_{F2}\sqrt{k_{20h}^2 + k_{yh}^{*2}}$.

To estimate characteristic values, we consider the planar heterostructure combining a gapless nanoribbon with gapped graphene sheets with $\Delta_1 = 0.75$ eV, $v_{F1} = 1.1v_{F2}$, $\Delta_3 = 1$ eV, and $v_{F3} = 1.2v_{F2}$. The nanoribbon width is $d = 2.46$ nm (ten hexagonal cells). Since the unknown values of V_1 and V_3 can be found by comparing our results with experimental data, we seek the dependence of energy spectrum parameters on V_1 and V_3. Note that $|V_1| \leq \Delta_1$ and $|V_3| \leq \Delta_3$ to ensure that the heterostructure is type I.

Figures 10–13 show the results of numerical calculations of electron and hole effective masses in the graphe-ne nanoribbon, extremum energies, k_{xe}^* and k_{xh}^* values, and pseudospin splitting $\delta E_s^{e,h}$ plotted versus work function for one of the gapped graphene sheets given that the work function for the other is zero.

It is clear from Fig. 13 that the pseudospin splitting energy may amount to approximately 10 meV. To obtain a larger pseudospin splitting, QW must be more asymmetric. Both V_1 and V_3 can be varied by shifting the valley energies in gapped graphene under applied stress, with potential barriers playing the role of bandgaps in the gapped graphene sheets. An analogous effect is achieved by applying an electric field on the order of 10^6 V/cm perpendicular to the interfaces in the graphene plane [33].

As expected, the energy spectrum is symmetric under the change $E \to -E$ when V_1 and $V_3 = 0$; i.e., the electron and hole spectra have equal effective masses, extremum energies, extremum positions, and pseudospin splitting energies. The electron and hole effective masses in graphene are smaller than those in the gapped graphene sheets adjoining the gapless graphene nanoribbon ($m_1^* = \Delta_1/v_{F1}^2 \approx 0.11m_0$ and $m_3^* = \Delta_3/v_{F3}^2 \approx 0.15m_0$).
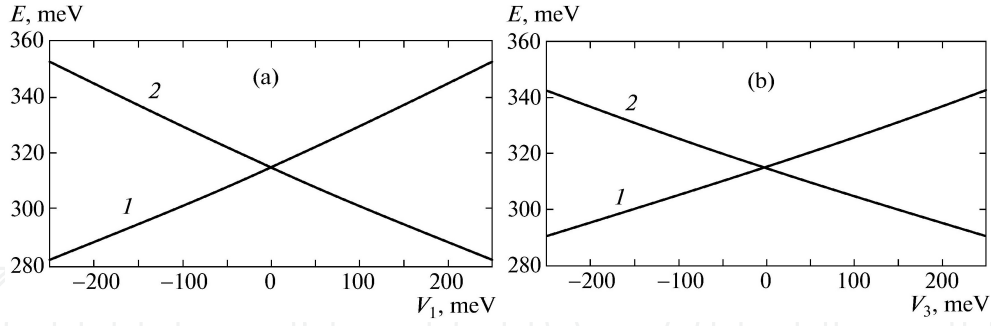
Figure 11. Electron (curves *1*) and hole (curves *2*) extremum energies and in the size-quantization spectra as functions of V_1 for $V_3 = 0$ **(a)** and as functions of V_3 for $V_1 = 0$ **(b)**. The effective bandgap $E_g^{eff} = E_0^e + |E_0^h| \approx 629$ meV varies insignificantly.
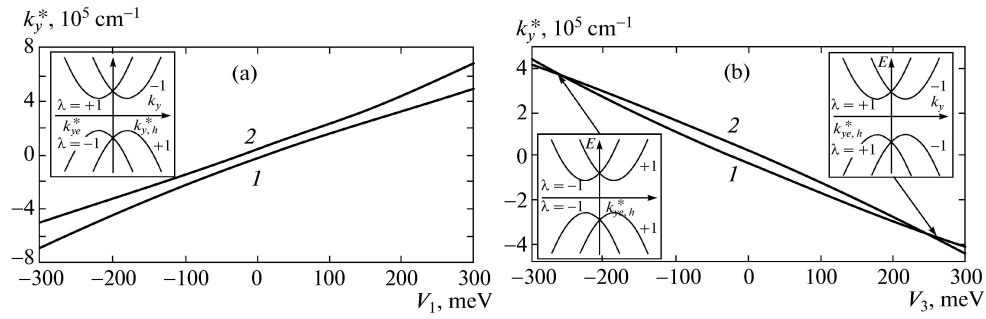
Figure 12. Extremum points of size-quantization branches for electrons ($k_y^* = k_{ye}^*$, curves *1*) and holes ($k_y^* = k_{yh}^*$, curves *2*) as functions V_1 for $V_3 = 0$ **(a)** and as functions of V_3 for $V_1 = 0$ **(b)**. Inserts show the relative positions of dispersion curves for $V_1 = V_3 = 0$ **(a)** and at $k_{ye}^* = k_{yh}^*$ **(b)**; K and K' points are set at the same position for simplicity.
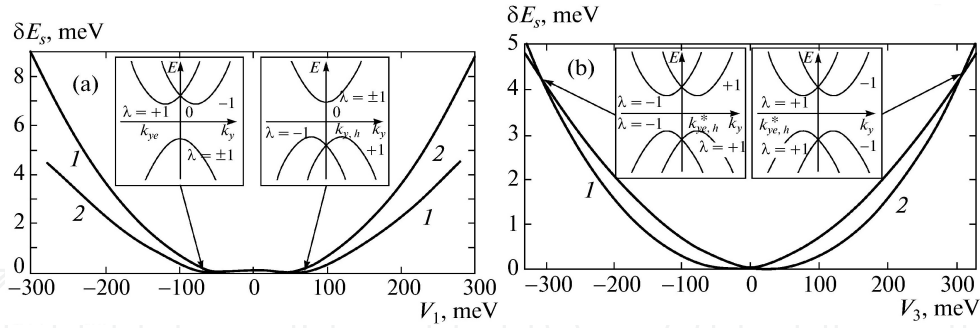
Figure 13. Pseudospin splitting in electron (curves *1*) and hole (curves *2*) spectra, δE_s^e and δE_s^h, as functions V_1 for $V_3 = 0$ **(a)** and as functions of V_3 for $V_1 = 0$ **(b)**. Vanishing $\delta E_s^{e,h}$ corresponds to vanishing $k_{ye,h}^*$ in Fig. 8, as shown in inserts to **(a)**. Inserts to **(b)** show positions of dispersion curves when k_{ye}^* and k_{yh}^* coincide.

4.3. Interface states

We consider interface states of a new type that arise in a narrow quasimomentum interval from the crossing of dispersion curves and are analogous to those in narrow-gap semiconductor heterostructures [44]. In the planar graphene-based heterostructure examined here, these states are localized near the heterojunction interfaces between the nanoribbon and the gapped graphene sheets. Interface states can exist not only in QWs but also in quantum

barriers [10]. Note that interface states arise as well from the crossing of dispersion curves in a single heterojunction between different graphene materials [42].

The wave function describing an interface electronic state is expressed as follows.

1. At $x < 0$,

$$\widetilde{\psi}_\lambda(x) = \widetilde{C} \begin{pmatrix} 1 \\ \widetilde{q}_1 \end{pmatrix} e^{\kappa_1 x},$$

(35)

where

$$\widetilde{q}_1 = -i \frac{u_1(\kappa_1 - \lambda k_y)}{E_\lambda - V_1 + \Delta_1},$$

$$v_{F1}\kappa_1 = \sqrt{\Delta_1^2 - (E_\lambda - V_1)^2 + v_{F1}^2 k_y^2}.$$

2. At $0 < x < d$,

$$\widetilde{\psi}_\lambda(x) = \widetilde{C} \begin{pmatrix} \widetilde{\varkappa}_- \\ \widetilde{q}_2 \widetilde{\varkappa}_- \end{pmatrix} e^{-\kappa_2 x} + \widetilde{C} \begin{pmatrix} \widetilde{\varkappa}_+ \\ \widetilde{q}_2' \widetilde{\varkappa}_+ \end{pmatrix} e^{\kappa_2 x},$$

(36)

where

$$\widetilde{\varkappa}_\pm = \frac{1}{2} \sqrt{\frac{v_{F1}}{v_{F2}}} \left[1 \pm \frac{\lambda k_y}{\kappa_2} \pm \frac{v_{F1}(\kappa_1 - \lambda k_y)E_\lambda}{v_{F2}\kappa_2(E_\lambda - V_1 + \Delta_1)} \right],$$

$$\widetilde{q}_2 = i \frac{v_{F2}(\kappa_2 + \lambda k_y)}{E_\lambda}, \quad \widetilde{q}_2' = -i \frac{v_{F2}(\kappa_2 - \lambda k_y)}{E_\lambda}.$$

3. At $x > d$

$$\widetilde{\psi}_\lambda(x) = \widetilde{C} \begin{pmatrix} \widetilde{\zeta} \\ \widetilde{q}_3 \widetilde{\zeta} \end{pmatrix} e^{-\kappa_3(x-d)},$$

(37)

where

$$\widetilde{\zeta} = \sqrt{\frac{v_{F1}}{v_{F3}}} \left[ch(\kappa_2 d) + \left(\frac{\lambda k_y}{\kappa_2} + \frac{v_{F1}(\kappa_1 - \lambda k_y)E_\lambda}{v_{F2}\kappa_2(E_\lambda - V_1 + \Delta_1)} \right) sh(\kappa_2 d) \right]$$

$$\widetilde{q}_3 = i \frac{v_{F3}(\kappa_3 + \lambda k_y)}{E_\lambda - V_3 + \Delta_3},$$

$$v_{F3}k_3 = \sqrt{\Delta_3^2 - (E_\lambda - V_3)^2 + v_{F3}^2 k_y^2}.$$

The relation for energy of interface states is

$$E_\lambda = \pm v_{F2} \sqrt{k_y^2 - \kappa_2^2},$$

(38)

with plus and minus corresponding to electrons and holes, respectively.

The expression for energy in (38) implies that an interface state exists only if[4]

$$|\kappa_2| < |k_y|.$$

We obtain the dispersion relation

$$\tanh(\kappa_2 d) = v_{F2}\kappa_2 f(\lambda k_y; \kappa_1, \kappa_3, E_\lambda). \tag{39}$$

which is similar to (32) up to the substitutions $k_1 \to \kappa_1$, $k_2 \to i\kappa_2$, and $k_3 \to \kappa_3$.

When $V_1 = 0$, the allowed quasimomenta for hole interface states ($\lambda = -1$) are similar to those for electron states, but the hole and electron energies have opposite signs; i.e., the spectrum is symmetric under the change $E_\lambda \to -E_\lambda$. When $V_1 = 100$ meV, the symmetry is broken and hole interface states exist only at negative quasimomenta.

4.4. Excitons

In gapless graphene, the carrier effective mass is zero and excitons do not exist. The existence of excitons in gapless graphene would lead to excitonic instability and excitonic insulator transition to a gapped state [54, 55].

The energy gap arising in a graphene nanoribbon due to the size quantization makes it possible to generate excitons by optical excitation or electron-hole injection. Excitons in QW strongly affect optical properties of the system considered here.

Excitons in similar quasi-one-dimensional carbon-based systems (semiconducting single- and multi-walled nanotubes) have been studied theoretically in [56]. The exciton spectrum is calculated here for a planar graphene quantum well by using the model applied to quantum wires in [57]. This model yields simple analytical expressions for exciton binding energy.

Since formulas (33) and (34) are obtained in the nonrelativistic limit, the two-particle exciton wave function depending on the electron and hole coordinates y_- and y_+ in a sufficiently narrow nanoribbon must obey the 1D Schrödinger equation with Coulomb potential:

$$\left(-\frac{1}{2m_e^*}\frac{\partial^2}{\partial y_-^2} - \frac{1}{2m_h^*}\frac{\partial^2}{\partial y_+^2} - \frac{\widetilde{e}^2}{|y_- - y_+|} \right) \phi(y_-, y_+) = E'\phi(y_-, y_+), \tag{40}$$

where $E' = E - E_g^{eff}$ and $\widetilde{e}^2 \equiv e^2/\kappa_{eff}$. The effective dielectric constant of graphene, $\kappa_{eff} = (\varepsilon + \varepsilon')/2$, may vary widely with the dielectric constants ε and ε' of the media in contact with graphene, such as free-space permittivity and substrate dielectric constant [58, 59].

---

[4] The zero mode corresponding to $|\kappa_2| = |k_y|$ (with $E_\lambda = 0$) is irrelevant here because $\widetilde{\psi}_\lambda(x) \equiv 0$.

The electron-hole Coulomb interaction in a 1D graphene nanoribbon is three-dimensional, but the problem can be reduced to one dimension (electron and hole y positions) for sufficiently narrow nanoribbons.

Rewriting Eq. (40) in terms of electron-hole separation $y = y_- - y_+$ and center-of-mass coordinate

$$Y = \frac{m_e^* y_- + m_h^* y_+}{m_e^* + m_h^*}$$

and introducing the function

$$\phi(y_-, y_+) = \psi_n(y) e^{iKY},$$

where K is the total exciton momentum, we obtain

$$\left(-\frac{1}{2\mu^*} \frac{\partial^2}{\partial y^2} - \frac{\tilde{e}^2}{|y|} \right) \psi_n(y) = E_n \psi_n(y), \tag{41}$$

where $\mu^* = m_e^* m_h^* / (m_e^* + m_h^*)$ is the reduced mass and E_n is the energy of the nth exciton level ($n = 0, 1, 2, \ldots$ is the principal quantum number). The total exciton energy E' is obtained by adding the total kinetic energy of the electron-hole pair to E_n:

$$E' = E_n + \frac{K^2}{2(m_e^* + m_h^*)}.$$

To find the solution at $y > 0$, we substitute $\psi_n(y)$ represented as

$$\psi_n(y) = B_n \exp\left(-y/a_n\right) F_n\left(\frac{2y}{a_n}\right).$$

into Eq. (41) and obtain the confluent hypergeometric differential equation

$$\xi F_n'' - \xi F_n' + \eta F_n = 0, \tag{42}$$

where $\xi = \frac{2y}{a_n}$ and $\eta = \mu^* \tilde{e}^2 a_n$. We also have

$$E_n = -\frac{1}{2\mu^* a_n^2}. \tag{43}$$

Equation (42) with $\eta = n$ is solved by the associated Laguerre polynomial

$$F_n(\xi) = \frac{1}{n!} \xi e^{\xi} \frac{d^n}{d\xi^n} \left(\xi^{n-1} e^{-\xi} \right) \equiv L_n^{-1}(\xi).$$

and the wavefunction is expressed as

$$\psi_n(y) = B_n \exp\left(-y/a_n\right) L_n^{-1}\left(\frac{2y}{a_n}\right).$$

Analogously, we find the solution to Eq. (41) at $y < 0$:

$$\psi_n(y) = \pm B_n \exp\left(y/a_n\right) L_n^{-1}\left(-\frac{2y}{a_n}\right),$$

where "+" and "−" are taken for $n = 0$ and $n \neq 0$, respectively, and the continuity of $\psi_n(y)$ and its first derivative $\psi_n'(y)$ are used as boundary conditions. Since $\psi_n(0) = 0$ and $\psi'(0) \neq 0$ for $n \neq 0$, the excited-state wavefunction $\psi_n(y)$ is odd (otherwise, it would be discontinuous at the origin), whereas the ground-state wavefunction is even.

The normalization condition

$$\int\limits_{-\infty}^{\infty} |\psi_n(y)|^2 dy = 1$$

is used to determine the coefficient B_n in the expression for $\psi_n(y)$:

$$B_n = \left[a_n \int\limits_0^{\infty} (L_n^{-1}(\xi))^2 e^{-\xi} d\xi \right]^{-1/2}$$

and $B_n = 1/\sqrt{2a_n}$ for $n = 1, 2, \ldots$ and $B_0 = 1/\sqrt{a_0}$ for $n = 0$. Here,

$$a_n = \frac{n}{\mu^* \widetilde{e}^2} \tag{44}$$

($n = 1, 2 \ldots$) is the Bohr radius of an exciton in the nth excited state. Combining (43) with (44), we find the exciton energy spectrum:

$$E_n = -\frac{\mu^* \widetilde{e}^4}{2n^2}. \tag{45}$$

The 1D ground-state ($n = 0$) Coulomb energy exhibits a logarithmic divergence at short distances [60]. Therefore, the lateral spread of the exciton wave function (along the x axis) due to the three-dimensional nature of Coulomb interaction should be taken into account by introducing a cutoff parameter $d_0 \lesssim d$. Averaging the kinetic energy operator

$$\widehat{T} = -\frac{1}{2\mu^*}\frac{\partial^2}{\partial y^2}$$

and the potential

$$V(y) = -\frac{\tilde{e}^2}{|y|}\theta\left(|y| - d_0\right)$$

over ground-state wave functions

$$\psi_0(y) = \frac{1}{\sqrt{a_0}}e^{-|y|/a_0}, \tag{46}$$

where the ground-state Bohr radius a_0 plays the role of a variational parameter, we express the ground-state exciton energy as [42]

$$E_0 = \frac{1}{2\mu^* a_0^2} - \frac{2\tilde{e}^2}{a_0}\ln\frac{a_0}{d}. \tag{47}$$

Minimizing (47) with respect to a_0, we obtain an equation for a_0:

$$a_0 = \frac{a_1}{2\left(\ln\frac{a_0}{d} - 1\right)}. \tag{48}$$

To logarithmic accuracy, when

$$\ln\frac{a_1}{d} \gg 1, \tag{49}$$

we find the relations

$$E_0 = 4E_1\ln^2\frac{a_1}{d}, \tag{50}$$

$$a_0 = \frac{a_1}{2\ln\frac{a_1}{d}}. \tag{51}$$

Using (48), we easily obtain the next-order correction to E_0:

$$\delta E_0^{(1)} = -8E_1\ln\frac{a_1}{d}\ln\left(2\ln\frac{a_1}{d}\right).$$

We now examine the applicability of the formulas derived here. The semiconducting state induced in a graphene nanoribbon is stable with respect to spontaneous electron-hole pair creation (excitonic insulator transition) only if the exciton binding energy $|E_0|$ is smaller than the effective bandgap in the graphene nanoribbon,

$$|E_0| < E_g^{eff}.$$

Furthermore, the quantum well width d must be much smaller than the exciton Bohr radius a_1,

$$d \ll a_1.$$

Logarithmically accurate formula (50) is correct only if condition (49) holds. However, the asymmetric QW analyzed here to examine pseudospin effects may not admit even a single size-quantization level if the graphene nanoribbon width d is too narrow. As d decreases, the effective bandgap increases, approaching $\Delta_+ + \Delta_-$, where $\Delta_\pm = \min\{\Delta_1 \pm V_1, \Delta_3 \pm V_3\}$ (with plus and minus corresponding to electrons and holes, respectively). When a certain d_c is reached, the size-quantization levels are pushed into the continuum. This imposes a lower limit on d:

$$d > d_c,$$

where d_c can be estimated as [42]

$$d_c \simeq \frac{\pi v_{F2}}{\Delta_+ + \Delta_-}.$$

As d increases, condition (49) is violated. In this case, a more accurate variational calculation should be performed using the modified three-dimensional Coulomb potential

$$\widetilde{V}(y) = -\frac{\widetilde{e}^2}{\sqrt{y^2 + d_0^2}},$$

where d_0 is a cutoff parameter. We average the Hamiltonian with potential $\widetilde{V}(y)$ over trial functions (46) to obtain

$$E_0 = \frac{1}{2\mu^* a_0^2} - \frac{2\widetilde{e}^2}{a_0} I(\rho), \tag{52}$$

where $I(\rho) = \frac{\pi}{2}[H_0(\rho) - Y_0(\rho)]$, $H_\nu(\rho)$ is a Struve function, $Y_\nu(\rho)$ is a Bessel function of the second kind, and $\rho = 2d_0/a_0$ (ν is 0 here and 1 below).

Minimizing (52) with respect to a_0, we obtain an equation for a_0:

$$\frac{2a_0}{a_1} I(\rho) + \frac{4d_0}{a_1} J(\rho) = 1, \tag{53}$$

where $J(\rho) = 1 - \frac{\pi}{2}[H_1(\rho) - Y_1(\rho)]$.

Figure 14 shows the numerical results obtained by using both methods to calculate $E_0(d)$ for the heterostructure, with $d_0 \propto d$ adjusted to match the curves at small d. Discrepancy at large d increases as $\ln(a_1/d)$ approaches unity.
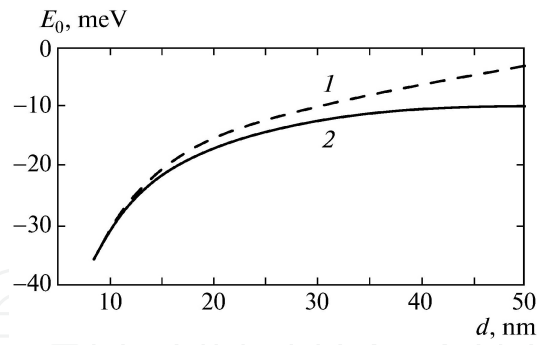
Figure 14. Exciton ground-state energy calculated by formula (50) (curve *1*) and by formula (52) after Eq. (53) is solved numerically for a_0 (curve *2*), $d_0 = 0.22d$.

4.5. Electric field effect on excitons levels

Interaction between an exciton and an external electrostatic field $\mathcal{E}$ is described by the operator

$$\widehat{H}_i = -\mathbf{d}\boldsymbol{\mathcal{E}} = |\widetilde{e}|(\mathcal{E}_x x + \mathcal{E}_y y)$$

where $x = |x_- - x_+|$ and $y = |y_- - y_+|$ are the electron-hole relative position vector components and $\mathbf{d}$ is dipole moment. The electric field is supposed to be weak enough to ensure that the energy level shift is not only smaller than the spacing between size-quantization levels but also smaller than the spacing between exciton levels. These conditions can be written as

$$d \ll a_1 \ll a_{\mathcal{E}},$$

where $a_{\mathcal{E}} = (\mu^* |\widetilde{e}|\mathcal{E})^{-1/3}$ is the electric length.

We consider two cases: (1) the electric field is applied parallel to the x axis and perpendicular to the nanoribbon edges in the graphene plane; (2) the electric field is applied along the y axis, parallel to the nanoribbon edges.

In the former case, the energy shift varies linearly with the difference between the average x components of the electron and hole position vectors:

$$E^{(1)}_{\perp \lambda \lambda'} = |\widetilde{e}|\mathcal{E}\left(\langle x_-\rangle_\lambda - \langle x_+\rangle_{\lambda'}\right), \tag{54}$$

where average x components are calculated by using electron and hole single-particle wave functions, generally depending on the electron and hole eigenvalues λ and λ' of the operator $\widehat{P}$, respectively. Exciton energy shift (54) is independent of the principal quantum number n. It may vary with λ and λ', resulting in different exciton binding energies (more precisely, the binding energy of an electron–hole pair with $\lambda = \pm 1$ and $\lambda' = \pm 1$ may have four different values).

In the latter case, the first-order electric field-induced correction is zero[5],

---

[5] Note that $E^{(1)}_{\perp n} \equiv 0$ in the former case if the electron and hole spectra transform into each other under field inversion.

$$E_{\|n}^{(1)} = |\widetilde{e}|\mathcal{E}\langle y\rangle_n \equiv 0, \tag{55}$$

because the integral of $y|\psi_n(y)|^2$ with respect to y vanishes. To evaluate the second-order electric field-induced correction, we make use of the Dalgarno–Lewis perturbation theory [61]. Defining a Hermitian operator such that

$$[\widehat{F}, \widehat{H}_0]|n\rangle = \widehat{H}_i|n\rangle, \tag{56}$$

where

$$\widehat{H}_0 = -\frac{1}{2\mu^*}\frac{\partial^2}{\partial y^2} - \frac{\widetilde{e}^2}{|y|}$$

is the zeroth-order Hamiltonian, $|n\rangle = \psi_n(y)$ is the zeroth-order wave function of the nth exciton level, and $\widehat{H}_i = |\widetilde{e}|\mathcal{E}y$, we obtain

$$E_{\|n}^{(2)} = \langle n|\widehat{H}_i\widehat{F}|n\rangle - \langle n|\widehat{H}_i|n\rangle\langle n|\widehat{F}|n\rangle. \tag{57}$$

In the case in question, the second term in this formula vanishes by virtue of (55).

Rewriting Eq. (56) as

$$\psi_n\frac{\partial^2\widehat{F}}{\partial y^2} + 2\frac{\partial\psi_n}{\partial y}\frac{\partial\widehat{F}}{\partial y} = 2\mu^*\widehat{H}_i\psi_n, \tag{58}$$

we find

$$\widehat{F}(y) = 2\mu^*\int\limits_{-\infty}^{y}\frac{dy'}{|\psi_n(y')|^2}\int\limits_{-\infty}^{y'}dy''\psi_n^*(y'')\widehat{H}_i\psi_n(y''). \tag{59}$$

Combining (57) with (59), we have the exciton ground-state energy shift [42]

$$E_{\|0}^{(2)} = -\frac{5}{128}\frac{a_1^3}{\ln^4\frac{a_1}{d}}\mathcal{E}^2, \tag{60}$$

which is very small compared to E_0 given by (50) because of the fourth power of a logarithm in the denominator and a small numerical factor.

For comparison, we write out the energy correction to the first excited exciton state [42]

$$E_{\|1}^{(2)} = -\frac{3}{8}(31 - 6\gamma)a_1^3\mathcal{E}^2,$$

where $\gamma = 0.577\ldots$ is Euler's constant.

By analogy with layered heterostructures [62], the ionizing (exciton-breaking) field strength $\mathcal{E}_c$ is estimated as

$$\mathcal{E}_c = \frac{|E_0|}{8|\tilde{e}|\langle|y|\rangle_0},$$

(61)

where $\langle|y|\rangle_0 = a_0/2$ is the average electron-hole separation for the ground-state exciton. To logarithmic accuracy, it follows that [42]

$$\mathcal{E}_c = \mu^{*2}|\tilde{e}|^5 \ln^3 \frac{a_1}{d}.$$

(62)

To get the order of magnitude of $\mathcal{E}_c$, consider QW discussed abode. Setting $m_e^* = m_h^* \approx 0.0056m_0$, the SiO_2 substrate dielectric constant $\kappa_{eff} \approx 5$, $d = 2.46$ nm, and $a_1 \approx 81$ nm, we use formula (62) to obtain $\mathcal{E}_c = 9$ kV/cm.

4.6. The effective theory

4.6.1. The effective Hamiltonian

According to the expressions (33) and (34) we have the approximations for dispersion curves of electrons and holes respectively

$$E_\lambda^e \approx E_0^e + \frac{1}{2m_e^*}\left(k_y - \lambda k_{ye}^*\right)^2 = \frac{k_y^2}{2m_e^*} - \lambda\alpha_e k_y + \Delta_e \equiv \widetilde{E}_\lambda^e,$$

$$E_\lambda^h \approx E_0^h - \frac{1}{2m_h^*}\left(k_y + \lambda k_{yh}^*\right)^2 = -\frac{k_y^2}{2m_h^*} - \lambda\alpha_h k_y + \Delta_h \equiv \widetilde{E}_\lambda^h,$$

(63)

where the following notations are introduced

$$\alpha_{e,h} = \frac{k_{ye,h}^*}{m_{e,h}^*}, \quad \Delta_{e,h} = \pm\frac{k_{ye,h}^{*2}}{2m_{e,h}^*} + E_0^{e,h}$$

(in the latter formula plus corresponds to the case of electrons, minus for the case of holes).

We can write the effective Hamiltonians in the form including explicitly the parity λ

$$\widehat{H}_{eff}^{(\lambda)e} = \frac{\widehat{p}_y^2}{2m_e^*} - \lambda\alpha_e\widehat{p}_y + \Delta_e,$$

$$\widehat{H}_{eff}^{(\lambda)h} = \frac{\widehat{p}_y^2}{2m_h^*} - \lambda\alpha_h\widehat{p}_y + \Delta_h.$$

(64)

We can also combine the Hamiltonians $\widehat{H}_{eff}^{(+1)e}$ and $\widehat{H}_{eff}^{(-1)e}$ into one 2×2 matrix Hamiltonian (analogously for $\widehat{H}_{eff}^{(+1)h}$ and $\widehat{H}_{eff}^{(-1)h}$)

$$\begin{aligned}
\widehat{H}_{eff}^e &= \frac{\hat{p}_y^2}{2m_e^*} - \alpha_e \tau_z \hat{p}_y + \Delta_e, \\
\widehat{H}_{eff}^h &= \frac{\hat{p}_y^2}{2m_h^*} - \alpha_h \tau_z \hat{p}_y + \Delta_h.
\end{aligned} \tag{65}$$

Here we emphasize by using the matrix τ_z that these Hamiltonians act in the valley space. The eigen wave functions of these Hamiltonians $\widetilde{\Psi}_\lambda^e$ and $\widetilde{\Psi}_\lambda^h$,

$$\widehat{H}_{eff}^e \widetilde{\Psi}_\lambda^e = \widetilde{E}_\lambda^e \widetilde{\Psi}_\lambda^e \text{ and } \widehat{H}_{eff}^h \widetilde{\Psi}_\lambda^h = \widetilde{E}_\lambda^h \widetilde{\Psi}_\lambda^h,$$

are spinors in a class of eigen functions of the operator $\widehat{\mathcal{P}} = \tau_z$ which can be considered as a "reduced" parity operator:

$$\begin{aligned}
\widehat{\mathcal{P}} \widetilde{\Psi}_\lambda^{e,h} &= \lambda \widetilde{\Psi}_\lambda^{e,h}, \\
\widetilde{\Psi}_{+1}^{e,h} = \begin{pmatrix} \widetilde{\psi}_{+1}^{e,h} \\ 0 \end{pmatrix}, \quad \widetilde{\Psi}_{-1}^{e,h} &= \begin{pmatrix} 0 \\ \widetilde{\psi}_{-1}^{e,h} \end{pmatrix}.
\end{aligned} \tag{66}$$

(Remember that the parity operator $\widehat{P} = \tau_z \otimes \sigma_0$ where the matrix σ_0 acts in the sublattice space.)

We can also see that the second term in (65) is an analogue of spin-orbit (SO) coupling in the Rashba form:

$$\widehat{H}_{SO}^{e,h} = \alpha_{e,h} [\boldsymbol{\tau} \widehat{\mathbf{p}}] \cdot \boldsymbol{\nu}, \tag{67}$$

where $\boldsymbol{\tau} = (\tau_x, \tau_y, \tau_z)$ is the matrix vector in the valley space ($\boldsymbol{\tau}$ is the pseudospin operator), $\widehat{\mathbf{p}} = (\widehat{p}_x, \widehat{p}_y, 0)$ is the vector operator of momentum in the xy-plane, and $\boldsymbol{\nu}$ is the unit vector of the normal to the heterojunction interface (in the coordinate system used here, $\boldsymbol{\nu} = \mathbf{e}_x$ is the unit coordinate vector of the x axis). The constants $\alpha_{e,h}$ can be named as the effective Rashba constants.

So, we have the effective theory with the non-relativistic Hamiltonian with the SO-like term describing the pseudospin splitting of the energy spectrum of charge carriers. An appearance of this term is due to an asymmetry of a QW potential profile. In an absence of the asymmetry in the case of the symmetrical QW, the effective Rashba constants $\alpha_{e,h}$ tend to zero for both electrons and holes and there is no the pseudospin splitting in its energy spectra.

4.6.2. The effective Hamiltonian in a presence of a magnetic field

Let us set a problem about a quantization of a charge carriers energy in the planar heterostructure based on graphene in a magnetic field applied perpendicular to its plane. To begin with, we make some remarks.

Firstly, to separate the size quantization and the magnetic field quantization, we assume that a magnetic field H is enough weak one. Its condition can be expressed as the following inequality

$$a_H \gg d, \tag{68}$$

where

$$a_H = \sqrt{\frac{c}{|e|H}}$$

is the magnetic length, i.e. a restriction of the wave function along the y axis due to a magnetic field is significantly smaller than its restriction along the x axis (perpendicular to the potential barriers). A complexity of the problem consists in an absence of the usual Landau quantization whereas we have it in layered heterostructures at an application of a magnetic field perpendicular to layers (in this case problems about the size quantization and the magnetic field quantization are automatically separated).

Secondly, a vector potential $\mathbf{A}$ must be chosen so that decreasing wave function $\widetilde{\Psi}_\lambda^{e,h}(x, y)$ in the direction of the y axis is taken into account in an explicit form. The equation for $\widetilde{\Psi}_\lambda^{e,h}(x, y)$ in a presence the of a magnetic field must include a y coordinate. From general considerations, it is clear that $\widetilde{\Psi}_\lambda^{e,h}(x, y)$ must decrease along the y axis on the scale of a_H (see the schematic picture on Fig. 15).

An appropriate choice of the vector potential is

$$\mathbf{A} = (-Hy, 0, 0).$$

To have an opportunity to make the minimal substitution, the effective equation for $\widetilde{\Psi}_\lambda^{e,h}(x, y)$ must explicitly contain the momentum operator $\widehat{p}_x$. However, this operator was excluded from the effective Hamiltonian without a magnetic field (65). This circumstance makes us detach in the effective equation an artificial term corresponding to the "size-quantization energy" $E_0^{e,h}$ so that

$$\frac{\widehat{p}_x^2}{2m_{e,h}^*} \widetilde{\Psi}_\lambda^{e,h}(x, y) = E_0^{e,h} \widetilde{\Psi}_\lambda^{e,h}(x, y).$$

Moreover, we propose to use an approximate expression

$$E_0^{e,h} = \pm \frac{k_{xe,h}^{*2}}{2m_{e,h}^*},$$
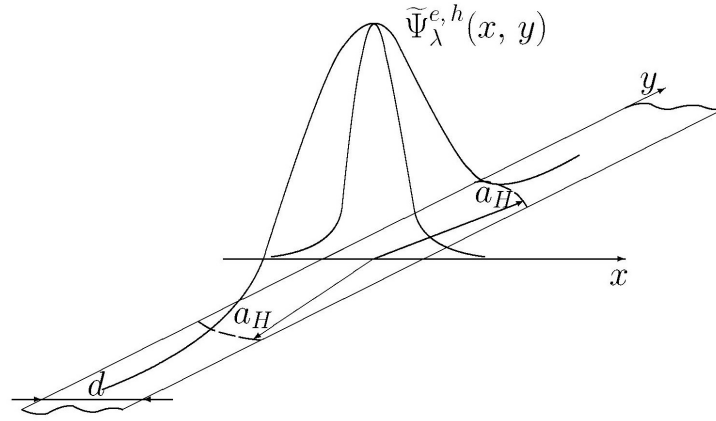
Figure 15. A behavior of the envelope wave function $\widetilde{\Psi}_\lambda^{e,h}(x, y)$ of charge carriers in the planar heterostructure in a presence of a magnetic field applied perpendicular to its plane.

where k_{xe}^* and k_{xh}^* are the size-quantized values of k_x as eigen values of the operator $\widehat{p}_x$ for electrons and holes near the extrema $k_y = \lambda k_{ye}^*$ and $k_y = -\lambda k_{yh}^*$, respectively.

So, we have in a presence of a magnetic field

$$
\begin{aligned}
\widehat{H}_{eff}^{\prime e} &= \frac{1}{2m_e^*}\left(k_{xe}^* + \frac{e}{c}Hy\right)^2 + \frac{1}{2m_e^*}\widehat{p}_y^2 + \widehat{H}_{SO}^e + \widetilde{\Delta}_e, \\
\widehat{H}_{eff}^{\prime h} &= \frac{1}{2m_h^*}\left(k_{xh}^* + \frac{e}{c}Hy\right)^2 + \frac{1}{2m_h^*}\widehat{p}_y^2 + \widehat{H}_{SO}^h + \widetilde{\Delta}_h,
\end{aligned}
\tag{69}
$$

with

$$
\widetilde{\Delta}_{e,h} = \pm\frac{k_{ye,h}^{*2}}{2m_{e,h}^*}.
$$

We can introduce operators of a generalized momentum in a magnetic field

$$
\begin{aligned}
\widehat{P}_x^{e,h} &= k_{xe,h}^* - \frac{e}{c}\mathcal{A}_x, \\
\widehat{P}_y^{e,h} &= \widehat{p}_y - \frac{e}{c}\mathcal{A}_y.
\end{aligned}
\tag{70}
$$

The operators $\widehat{P}_x^{e,h}$ are c-numbers, whereas the operators $\widehat{P}_y^{e,h}$ coincide with the differential operator $\widehat{p}_y = -i\partial_y$ in the determined above vector potential **A**. The commutation relation for these operators is

$$
\left[\widehat{P}_x^{e,h}, \widehat{P}_y^{e,h}\right] = \frac{ie}{c}H.
\tag{71}
$$

We can also consider the combinations of these operators

$$\widehat{P}_{\pm}^{e,h} = \widehat{P}_x^{e,h} \pm i\widehat{P}_y^{e,h} \tag{72}$$

with the commutation relation

$$\left[\widehat{P}_-^{e,h}, \widehat{P}_+^{e,h}\right] = -\frac{2e}{c}H. \tag{73}$$

Following the Rashba's paper [63] we can introduce the annihilation and creation operators: for electrons as

$$\hat{a}_e = \sqrt{\frac{c}{2|e|H}}\widehat{P}_-^e, \ \hat{a}_e^{\dagger} = \sqrt{\frac{c}{2|e|H}}\widehat{P}_+^e,$$

for holes as

$$\hat{a}_h = \sqrt{\frac{c}{2|e|H}}\widehat{P}_+^e, \ \hat{a}_h^{\dagger} = \sqrt{\frac{c}{2|e|H}}\widehat{P}_-^h$$

with the Bose commutation relation

$$\left[\hat{a}_{e,h}, \hat{a}_{e,h}^{\dagger}\right] = 1.$$

The effective Hamiltonians rewritten in the second-quantized representation are

$$\widehat{H}_{eff}''^{e} = \omega_c^{*e}\left(\hat{a}_e^{\dagger}\hat{a}_e + \frac{1}{2}\right) - \frac{i}{\sqrt{2}}\frac{\alpha_e}{a_H}\tau_z\left(\hat{a}_e - \hat{a}_e^{\dagger}\right) + \widetilde{\Delta}_e,$$

$$\widehat{H}_{eff}''^{h} = \omega_c^{*h}\left(\hat{a}_e^{\dagger}\hat{a}_e + \frac{1}{2}\right) + \frac{i}{\sqrt{2}}\frac{\alpha_h}{a_H}\tau_z\left(\hat{a}_h - \hat{a}_h^{\dagger}\right) + \widetilde{\Delta}_h, \tag{74}$$

where $\omega_c^{*e,h} = \frac{|e|H}{m_{e,h}^*c}$ are the cyclotron frequencies.

Let us solve the equation for $\widetilde{\Psi}_{\lambda}^{e,h}$ with the Hamiltonians (74) in the class of eigen functions of the operator $\widehat{\mathcal{P}}$. The matrix τ_z should be replaced by corresponding eigen value λ in the equations for the components of $\widetilde{\Psi}_{\lambda}^{e,h}$. After a nondimensionalization, these equations are written as

$$\left[\hat{a}_e^{\dagger}\hat{a}_e + \frac{1}{2} - i\lambda\delta_{SO}^e\left(\hat{a}_e - \hat{a}_e^{\dagger}\right)\right]\widetilde{\psi}_{\lambda}^e = \epsilon_{\lambda}^e\widetilde{\psi}_{\lambda}^e,$$

$$\left[\hat{a}_h^{\dagger}\hat{a}_h + \frac{1}{2} + i\lambda\delta_{SO}^h\left(\hat{a}_h - \hat{a}_h^{\dagger}\right)\right]\widetilde{\psi}_{\lambda}^h = \epsilon_{\lambda}^h\widetilde{\psi}_{\lambda}^h, \tag{75}$$

where $\delta_{SO}^{e,h} = \frac{\alpha_{e,h}}{\sqrt{2}a_H\omega_c^{*e,h}} = \frac{1}{\sqrt{2}}a_H k_{ye,h}^*$ and $\pm\epsilon_\lambda^{e,h} = \frac{E_\lambda^{e,n}-\Delta_{e,h}}{\omega_c^{*e,h}}$, $\epsilon_\lambda^{e,h} > 0$ and plus corresponds to electrons (its energy $\widetilde{E}^e = \widetilde{\Delta}_e + \omega_c^{*e}\epsilon_\lambda^e$ has positive values), minus corresponds to holes (its energy $\widetilde{E}^h = \widetilde{\Delta}_h - \omega_c^{*h}\epsilon_\lambda^h$ has negative values).

Now we make an expansion of $\widetilde{\psi}_\lambda^{e,h}$ by the oscillator function basis ψ_n

$$\widetilde{\psi}_\lambda^{e,h} = \sum_{n=0}^\infty a_{\lambda n}^{e,h}\psi_n. \tag{76}$$

We have also the normalization condition in the form of the integral

$$\int_{-\infty}^\infty \left|\widetilde{\psi}_\lambda^{e,h}\right|^2 dy = 1$$

or in the form of the series

$$\sum_{n=0}^\infty \left|a_{\lambda n}^{e,h}\right|^2 = 1. \tag{77}$$

Taking into account the relations

$$\hat{a}_{e,h}\psi_n = \sqrt{n}\psi_{n-1},$$
$$\hat{a}_{e,h}^\dagger\psi_n = \sqrt{n+1}\psi_{n+1},$$

we obtain two infinite systems of equations for coefficients $a_{\lambda n}^e$ and $a_{\lambda n}^h$

$$\begin{cases} \dfrac{1}{2}a_{\lambda 0}^e - i\lambda\delta_{SO}^e a_{\lambda 1}^e = \epsilon_\lambda^e a_{\lambda 0}^e, \\[2mm] \dfrac{3}{2}a_{\lambda 1}^e - i\lambda\sqrt{2}\delta_{SO}^e a_{\lambda 2}^e + i\lambda\delta_{SO}^e a_{\lambda 0}^e = \epsilon_\lambda^e a_{\lambda 1}^e, \\[2mm] \dfrac{5}{2}a_{\lambda 2}^e - i\lambda\sqrt{3}\delta_{SO}^e a_{\lambda 3}^e + i\lambda\sqrt{2}\delta_{SO}^e a_{\lambda 1}^e = \epsilon_\lambda^e a_{\lambda 2}^e, \\[2mm] \cdots\cdots\cdots\cdots\cdots\cdots\cdots\cdots\cdots\cdots\cdots\cdots\cdots\cdots\cdots \\[2mm] \left(n + \dfrac{1}{2}\right)a_{\lambda n}^e - i\lambda\sqrt{n+1}\delta_{SO}^e a_{\lambda n+1}^e + i\lambda\sqrt{n}\delta_{SO}^e a_{\lambda n-1}^e = \epsilon_\lambda^e a_{\lambda n}^e, \\[2mm] \cdots\cdots\cdots\cdots\cdots\cdots\cdots\cdots\cdots\cdots\cdots\cdots\cdots\cdots\cdots \end{cases} \tag{78}$$

$$\begin{cases} \dfrac{1}{2}a^h_{\lambda 0} + i\lambda\delta^h_{SO}a^h_{\lambda 1} = \epsilon^h_\lambda a^h_{\lambda 0}, \\[2mm] \dfrac{3}{2}a^h_{\lambda 1} + i\lambda\sqrt{2}\delta^h_{SO}a^h_{\lambda 2} - i\lambda\delta^h_{SO}a^h_{\lambda 0} = \epsilon^h_\lambda a^h_{\lambda 1}, \\[2mm] \dfrac{5}{2}a^e_{\lambda 2} + i\lambda\sqrt{3}\delta^h_{SO}a^h_{\lambda 3} - i\lambda\sqrt{2}\delta^h_{SO}a^h_{\lambda 1} = \epsilon^h_\lambda a^h_{\lambda 2}, \\[2mm] \text{..} \\[2mm] \left(n + \dfrac{1}{2}\right)a^h_{\lambda n} + i\lambda\sqrt{n+1}\,\delta^h_{SO}a^h_{\lambda n+1} - i\lambda\sqrt{n}\,\delta^h_{SO}a^h_{\lambda n-1} = \epsilon^h_\lambda a^h_{\lambda n}, \\[2mm] \text{..} \end{cases} \tag{79}$$

On the other hand, it is clear from the physical considerations that the energy spectrum of charge carriers should be independent on the quasimomentum shift. Here, this shift equals to the position of the dispersion curve extrema $k_y = \pm k^*_{ye}$ for electrons and $k_y = \pm k^*_{yh}$ for holes. The Landau levels spectrum in (quasi)one-dimensional system should also be the same as it in the case when we choose the dispersion curve extrema as the point of reference for quasimomentum:

$$\epsilon^{e,h}_\lambda = n + \frac{1}{2}. \tag{80}$$

The systems of equations for coefficients $a^e_{\lambda n}$ (78) and $a^h_{\lambda n}$ (79) are the recurrence relations for a calculation of these coefficients. So, the dependence on the parameters δ^e_{SO} and δ^h_{SO} in the problem appears only in the wave function $\widetilde{\psi}^{e,h}_\lambda$.

Lastly, our remark concerns a matter about a convergence of the series (77). Each term $|a^{e,h}_{\lambda n}|^2$ contains a summand $\sim 1/(\delta^{e,h}_{SO})^{2n}$, therefore it is necessary $\delta^{e,h}_{SO} > 1$. This inequality should be valid due to the condition (68) because $k^*_{ye,h} \simeq 1/d$ for QW with enough strong asymmetry.

4.7. Possible experiments on the heterostructure

Pseudospin splitting can be observed by means of Raman spectroscopy. The D' peak of interest for the present study (alternatively called $2D$ peak to emphasize that it is due to a two-phonon-assisted process) is located at 2700 cm^{-1} [66]. It arises from intervalley scattering involving phonons with wavenumbers $q > K$, where $K = 4\pi/3\sqrt{3}a \approx 1.7 \times 10^8$ cm^{-1} is the spacing between adjacent K and K' points. One process of this kind is indicated as $A \to B \to C \to D \to A$ in Fig. 16.

Pseudospin splitting enables intervalley scattering involving phonons with $q' \approx q \mp \Delta k$ (with plus for electrons and minus for holes), where $\Delta k = 2k^*_{ye}$ and $\Delta k = 2k^*_{yh}$ in electron and hole scattering, respectively. These processes contribute to a peak blueshifted from D' by $\Delta\omega^{(+)}_R$ and a peak redshifted from D' by $\Delta\omega^{(-)}_R$, giving rise to a doublet structure of the D' peak.
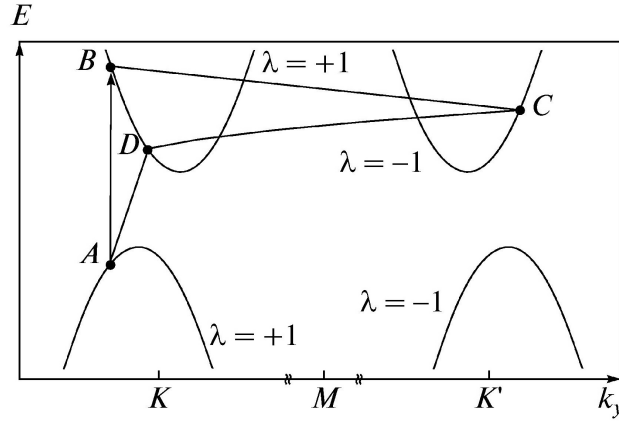
Figure 16. Possible double resonant Raman processes involving electron scattering between valleys. To simplify presentation, analogous processes involving hole scattering between valleys are not shown.

An estimate for $\Delta\omega_R$ can be obtained by using optical phonon dispersion $\omega_{ph}(q)$. The Raman shift is twice the optical phonon frequency:

$$\delta\omega_R(q) = 2\omega_{ph}(q).$$

The change in the Raman shift caused by pseudospin splitting is

$$\Delta\omega_R^{(\pm)} \approx |\delta\omega_R(\Delta K \mp \Delta k) - \delta\omega_R(\Delta K)|,$$

which amounts to $\Delta\omega_R \approx 24\ \mathrm{cm}^{-1}$ for characteristic values of the heterostructure parameters. This value essentially exceeds the Raman spectral resolution of $1\ \mathrm{cm}^{-1}$ [67] and compares to the D' peak width for gapless graphene, $\Gamma_0 = 30\ \mathrm{cm}^{-1}$ [68, 69].

Note that a blue shift of the D' peak has also been observed in the Raman spectrum of epitaxial graphene on a SiC substrate [67]. This effect is attributed to the strain induced by the substrate in quasi-free graphene since the SiC lattice constant exceeds substantially that of graphene.

Raman scattering contributions from gapped graphene sheets can be avoided either by using a laser beam whose width is smaller than that of the gapless graphene nanoribbon ($d \lesssim 10$ nm) or by pumping at a frequency ω such that the beam cannot be absorbed by gapped graphene materials,

$$E_g^{eff} + 2\omega_{ph} < \omega < min\{2\Delta_1, 2\Delta_3\}$$

The positions of the luminescence lines corresponding to exciton levels can be determined from optical experiments and compared to theoretical predictions. The splitting of exciton lines in an electric field applied in the plane of the heterostructure along the normal to its boundaries is evaluated by using formula (54).

Finally, interface states can manifest themselves in the I-V curve of the planar heterostructure carrying a current parallel to the gapless graphene nanoribbon.   An increase in applied electric field may cause charge carriers to "drop" into interface states (preferable energy-wise), giving rise to a region of negative differential conductivity in the I-V curve.

4.8. Some intermediate conclusions

Before proceeding to the next section, let us recall some results obtained in this section. We think that it is important for understanding the next results.

We have analyzed the characteristics of planar graphene nanostructures. On the one hand, they retain the unique properties of infinite graphene sheets. On the other hand, bandgap opening makes them important building blocks in carbon-based nanoelectronics, which can be used to control electron motion. Parameters of graphene QWs can easily be manipulated by varying the gapless nanoribbon width or the potential barriers in the adjoining gapped graphene sheets.

We predict pseudospin splitting to occur in asymmetric graphene QWs and interface states to arise from the crossing of dispersion curves of gapless and gapped graphene materials. We have performed calculations of optical properties of planar graphene nanostructures and suggested possible experiments to study the effects in question.

Analysis of pseudospin (valley) characteristics in the heterostructure is simplified by using an effective Hamiltonian having a pseudospin-split energy spectrum. Note that an analogous spectrum was discussed in [63–65]. Therefore, the effective Hamiltonian must contain a Rashba-like spin-orbit coupling. We have developed the effective theory for describing graphene-based systems with the pseudospin splitting.

5. Planar graphene superlattices

5.1. Superlattice based on graphene on a strip substrate

5.1.1. Some remarks

Interest in graphene-based superlattices (SL) has increased in recent years. Calculations of graphene-based SL with periodic rows of vacancies were performed using the molecular dynamics method [70]. Calculations of single-atom-thick SL formed by lines of pairs of adsorbed hydrogen atoms on graphene were carried out with the density functional theory [71].

Rippled graphene that can be treated as a SL with the one-dimensional periodic potential of ripples was investigated in [72–74]. SL obtained when a periodic electrostatic potential [75–78] or periodically located magnetic barriers [79–82] were applied to graphene were analytically examined.

However, the investigation of the graphene-based SL with a periodic electrostatic potential disregarded the fact that the application of the electrostatic potential to a gapless semiconductor (graphene) results in the production of electron-hole pairs and the redistribution of charges: electrons move from the region where the top of the valence band lies above the Fermi level to the region where the bottom of the conduction band lies
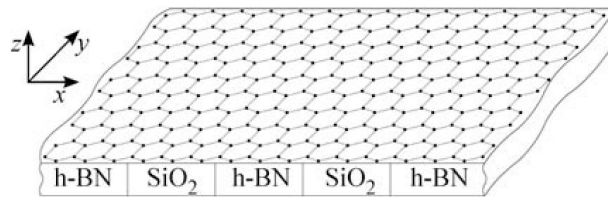
Figure 17. Graphene on the strip substrate consisting of alternating SiO$_2$ and h-BN strips.

below the Fermi level. The SL becomes a structure consisting of positively charged regions, where the electrostatic potential displacing the Dirac points upward in energy is applied, alternating with negatively charged regions. The strong electrostatic potential of induced charges appears and strongly distorts the initial step electrostatic potential and, therefore, the electronic structure of SL calculated disregarding the electrostatic potential of induced charges.

To avoid the production of electron-hole pairs, SL appearing due to the periodic modulation of the band gap is considered.

SL in the form of the periodic planar heterostructure of graphene nanoribbons between which nanoribbons of h-BN are inserted was previously proposed in [83]. The band structure of such SL was numerically calculated. However, it is very difficult to implement this SL even using the advances of modern lithography, because problems inevitably arise with the control of periodicity in the process of the etching of nanoribbons in a graphene sheet and the insertion of h-BN nanoribbons. Moreover, h-BN is an insulator with a band gap of 5.97 eV, which significantly hinders the tunneling of carriers between graphene nanoribbons. Such a heterostructure is most probably a set of QWs where the wavefunctions of carriers from neighboring QWs almost do not overlap.

Here, SL formed by a graphene sheet deposited on a strip substrate is proposed. The strip substrate is made of periodically alternating strips of SiO$_2$ (or any other material that does not affect the band structure of graphene) and h-BN, as shown in Fig. 17. The h-BN layers are located so that its hexagonal crystal lattice is under the hexagonal crystal lattice of graphene. Owing to this location, a band gap of 53 meV appears in the band structure of graphene in the graphene-sheet regions under the h-BN layers [37, 84].

It is assumed that all of the contacts between the regions of different band gaps are first-kind contacts (Dirac points of graphene are located in the band gaps of the gap modification of graphene). Such SL is a first-type SL (classification of SL can be found, e.g., in [85]).

The main advantage of the proposed SL is the simplicity of the manufacture and control of its periodicity. It is worth noting that some problems can arise in SL. The difference between the lattice constants of h-BN and graphene is about 2% [37]. If about 100 hexagonal graphene cells are packed into one period of the superlattice, the formation of the band gap in the gap modification of graphene in the graphene sheet regions above h-BN is violated owing to the inaccurate arrangement of carbon atoms above boron or nitrogen atoms. Since contacts between graphene and its gap modification are not heterocontacts (contacts between substances with different chemical compositions), the edges of quantum wells can be insufficiently sharp and QWs cannot be considered as square QWs. A transient
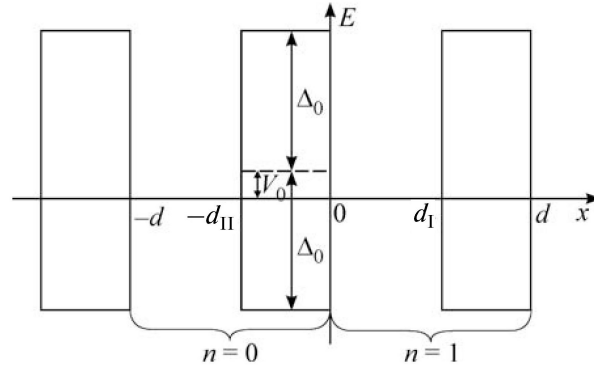
Figure 18. One-dimensional periodic Kronig-Penney potential of SL shown in Fig. 17: the periodically alternating gap modification of graphene on h-BN with a band gap of $2\Delta_0 = 53$ meV and gapless graphene on SiO$_2$.

layer with a spatially varying band gap can exist instead of the sharp edge. Finally, the substrate can be stressed. The appearing periodic stress field of the substrate can also affect the band structure of the proposed SL, but this effect is very small [86].

5.1.2. The model for describing SL

The x and y axes are perpendicular and parallel to the interfaces of h-BN and SiO$_2$ strips, respectively (see Fig. 16). SL is described by the Dirac equation

$$(v_F \boldsymbol{\sigma} \widehat{\mathbf{p}} + \Delta \sigma_z + V) \Psi(x\,y) = E\Psi(x, y), \tag{81}$$

where $v_F \approx 10^8$ cm/s is the Fermi velocity, $\boldsymbol{\sigma} = (\sigma_x, \sigma_y)$ and σ_z are the Pauli matrices, and $\widehat{\mathbf{p}} = -i\boldsymbol{\nabla}$ is the momentum operator (the system of units with $\hbar = 1$ is used). The half-width of the band gap is periodically modulated:

$$\Delta = \begin{cases} 0, & d(n-1) < x < -d_{II} + dn, \\ \Delta_0, & -d_{II} + dn < x < dn, \end{cases}$$

where n is an integer enumerating the supercells of the superlattice; d_I and d_{II} are the widths of the SiO$_2$ and h-BN strips, respectively; and $d = d_I + d_{II}$ are the period of the superlattice (the size of the supercell along the x axis). The periodic scalar potential V can appear due to the difference between the energy positions of the middle of the band gap of the gap modification of graphene and conic points of the Brillouin zone of gapless graphene (see Fig. 18):

$$V = \begin{cases} 0, & d(n-1) < x < -d_{II} + dn, \\ V_0, & -d_{II} + dn < x < dn. \end{cases}$$

In order for SL to be a first-type superlattice, the inequality $|V_0| \leq 0$ should be satisfied. The solution of Eq. (81) for the first supercell has the form

$$\Psi(x, y) = \psi_1(x) e^{ik_y y}, \qquad 0 < x < d.$$

For the nth supercell, in view of the periodicity of the superlattice,

$$\psi_n(x) = \psi_1(x + (n-1)d).$$

In the region of QW ($0 < x < d_I$), the solution of Eq. (81) is a plane wave

$$\psi_n^{(1)}(x) = N_{k_1} \begin{pmatrix} a_n^{(1)} \\ b_n^{(1)} \end{pmatrix} e^{ik_1 x} + N_{k_1} \begin{pmatrix} c_n^{(1)} \\ d_n^{(1)} \end{pmatrix} e^{-ik_1 x}, \tag{82}$$

where N_{k_1} is the normalization factor. The substitution of Eq. (82) into Eq. (81) provides the relation between the lower and upper spinor components

$$b_n^{(1)} = \lambda_+ a_n^{(1)}, \quad d_n^{(1)} = -\lambda_- c_n^{(1)}, \quad \lambda_\pm = \frac{v_F(k_1 \pm ik_y)}{E}.$$

The relation of E with k_1 and k_y has the form

$$E = \pm v_F \sqrt{k_1^2 + k_y^2}.$$

It is convenient to represent Eq. (82) in a more compact form [76]

$$\psi_n^{(1)}(x) = \Omega_{k_1}(x) \begin{pmatrix} a_n^{(1)} \\ c_n^{(1)} \end{pmatrix},$$

$$\Omega_{k_1}(x) = N_{k_1} \begin{pmatrix} 1 & 1 \\ \lambda_+ & -\lambda_- \end{pmatrix} e^{ik_1 x \sigma_z}. \tag{83}$$

When the inequality

$$\Delta_0^2 + v_F^2 k_y^2 - (E - V_0)^2 \geq 0 \tag{84}$$

is satisfied, the solution of Eq. (81) in the barrier region ($d_I < x < d$) has the form

$$\psi_n^{(2)}(x) = \Omega_{k_2}(x) \begin{pmatrix} a_n^{(2)} \\ c_n^{(2)} \end{pmatrix},$$

$$\Omega_{k_2}(x) = N_{k_2} \begin{pmatrix} 1 & 1 \\ -\tilde{\lambda}_- & \tilde{\lambda}_+ \end{pmatrix} e^{k_2 x \sigma_z}, \tag{85}$$

where

$$\widetilde{\lambda}_{\pm} = \frac{iv_F(k_2 \pm k_y)}{E + \Delta_0 - V_0}, \quad k_2 = \frac{1}{v_F}\sqrt{\Delta_0^2 + v_F^2 k_y^2 - (E - V_0)^2}.$$

The solution of Eq. (81) in the barrier region under the condition

$$\Delta_0^2 + v_F^2 k_y^2 - (E - V_0)^2 < 0 \tag{86}$$

is given by Eq. (85) with the change $k_2 \rightarrow i\varkappa_2$, i.e., it is oscillating.

The possibility of existing *Tamm* minibands formed by localized states near the interface between graphene and its gap modification will be considered below. In this case, $k_1 \rightarrow i\varkappa_1$ k_2 is real. A necessary condition for existing Tamm states has the form

$$|k_y| \geq |\varkappa_1|;$$

under this condition, the energy $E = \pm v_F \sqrt{k_y^2 - \varkappa_1^2}$ is real.

5.1.3. The derivation of the dispersion relation

The dispersion relation is derived using the transfer matrix (T matrix) method. The T matrix relates the spinor components for the nth supercell to the spinor components of the solution of the same type for the $(n + 1)$th supercell. For example, for the solution in the quantum well region,

$$\begin{pmatrix} a_{n+1}^{(1)} \\ c_{n+1}^{(1)} \end{pmatrix} = T \begin{pmatrix} a_n^{(1)} \\ c_n^{(1)} \end{pmatrix}. \tag{87}$$

To determine the T matrix, the following conditions of the continuity of the solution of the Dirac equation describing the considered superlattice are used:

$$\psi_n^{(1)}(d_I - 0) = \psi_n^{(2)}(d_I + 0),$$
$$\psi_n^{(2)}(d - 0) = \psi_{n+1}^{(1)}(+0).$$

These conditions provide the equalities

$$\begin{pmatrix} a_n^{(2)} \\ c_n^{(2)} \end{pmatrix} = \Omega_{k_2}^{-1}(d_I)\Omega_{k_1}(d_I)\begin{pmatrix} a_n^{(1)} \\ c_n^{(1)} \end{pmatrix},$$
$$\begin{pmatrix} a_{n+1}^{(1)} \\ c_{n+1}^{(1)} \end{pmatrix} = \Omega_{k_1}^{-1}(0)\Omega_{k_2}(d)\begin{pmatrix} a_n^{(2)} \\ c_n^{(2)} \end{pmatrix}.$$

According to definition (87) of the T matrix and the last two equalities[6],

$$T = \Omega_{k_1}^{-1}(0)\Omega_{k_2}(d)\Omega_{k_2}^{-1}(d_I)\Omega_{k_1}(d_I). \qquad (88)$$

The substitution of Eqs. (84) and (85) with the corresponding arguments into Eq. (88) yields the expressions

$$
\begin{aligned}
T_{11} &= \alpha e^{ik_1 d_I}\Big[(\lambda_- + \tilde{\lambda}_+)(\lambda_+ + \tilde{\lambda}_-)e^{-k_2 d_{II}} - \\
&\quad -(\lambda_- - \tilde{\lambda}_-)(\lambda_+ - \tilde{\lambda}_+)e^{k_2 d_{II}}\Big], \\
T_{12} &= 2\alpha e^{-ik_1 d_I}(\lambda_- + \tilde{\lambda}_+)(\lambda_- - \tilde{\lambda}_-)sh(k_2 d_{II}), \\
T_{21} &= T_{12}^*, \quad T_{22} = T_{11}^*,
\end{aligned}
\qquad (89)
$$

where

$$\alpha = \frac{1}{(\lambda_+ + \lambda_-)(\tilde{\lambda}_+ + \tilde{\lambda}_-)}.$$

The last two relations in Eqs. (89) are the general properties of the T matrix.

The derivation of the dispersion relation with the use of the T matrix is briefly as follows.

Let $N = L/d$ be the number of supercells in the entire SL, where L is the length of SL along the x axis, i.e., the direction of the application of the periodic potential. The Born-Karman cyclic boundary conditions for SL have the form

$$\psi_N^{(1,2)}(x) = \psi_1^{(1,2)}(x).$$

At the same time,

$$\psi_N^{(1,2)}(x) = T^N \psi_1^{(1,2)}(x),$$

from which, $T^N = \mathcal{I}$, where $\mathcal{I}$ is the 2×2 unit matrix.

It is convenient to diagonalize the T matrix by means of the transition matrix S:

$$T_d = STS^{-1} = \begin{pmatrix} \lambda_1 & 0 \\ 0 & \lambda_2 \end{pmatrix},$$

where $\lambda_{1,2}$ are the eigenvalues of the T matrix and have the property $\lambda_2 = \lambda_1^*$. According to $T_d^N = \mathcal{I}$

$$\lambda_1 = e^{2\pi i n/N}, \quad -N/2 < n \leq N/2.$$

---

[6] Note that the cyclic permutations of the factors of Ω matrices are possible in the definition of the T matrix; these permutation do not change dispersion relation (90). This can be verified by comparing Eq. (88) with Eq. (23) in [76].

In view of the property $TrT = TrT_d$ and in terms of the notation $k_x = 2\pi n/L$ ($-\pi/d < k_x \le \pi/d$), the dispersion relation is obtained in the form

$$TrT = 2\cos(k_x d). \qquad (90)$$

Taking into account the last relation in Eqs. (89), Eq. (90) can also be written in the form

$$ReT_{11} = \cos(k_x d).$$

Dispersion relation (90) under condition (84) gives the equation [86]

$$\frac{v_F^2 k_2^2 - v_F^2 k_1^2 + V_0^2 - \Delta_0^2}{2v_F^2 k_1 k_2} \sinh(k_2 d_{II})\sin(k_1 d_I) + \cosh(k_2 d_{II})\cos(k_1 d_I) = \cos(k_x d). \qquad (91)$$

According to this equation, the passage to the single-band limit is performed by two methods: first, $V_0 = \Delta_0$ (QW only for electrons) and, second, $V_0 = -\Delta_0$ (QW only for holes). The result of the passage coincides with the known nonrelativistic dispersion relation (see, e.g., [87]), although the expressions for k_1, k_2, and E are different.

If inequality (86) is satisfied, the change $k_2 \to i\varkappa_2$ should be made in Eq. (91)

$$\frac{-v_F^2 \varkappa_2^2 - v_F^2 k_1^2 + V_0^2 - \Delta_0^2}{2v_F^2 k_1 \varkappa_2} \sin(\varkappa_2 d_{II})\sin(k_1 d_I) + \cos(\varkappa_2 d_{II})\cos(k_1 d_I) = \cos(k_x d). \qquad (92)$$

For Tamm minibands, the change $k_1 \to i\varkappa_1$ should be made in Eq. (91):

$$\frac{v_F^2 k_2^2 + v_F^2 \varkappa_1^2 + V_0^2 - \Delta_0^2}{2v_F^2 \varkappa_1 k_2} \sinh(k_2 d_{II})\sinh(\varkappa_1 d_I) + \cosh(k_2 d_{II})\cosh(\varkappa_1 d_I) = \cos(k_x d). \qquad (93)$$

Equation (93) has the solution only under the condition

$$v_F^2 k_2^2 + v_F^2 \varkappa_1^2 + V_0^2 - \Delta_0^2 < 0.$$

This condition can be rewritten as

$$v_F^2 k_y^2 - E^2 < -EV_0. \qquad (94)$$

At the same time, for Tamm minibands $E^2 = v_F^2 k_y^2 - v_F^2 \varkappa_1^2$, i.e. the left-side of (94) is positive. The allowed values of the energy should be negative if $V_0 > 0$ and vice versa. It is not difficult to show that the inequality (94) has the solutions when [88]

$$v_F^2 k_y^2 < \frac{\Delta_0^2(\Delta_0^2 - V_0^2)}{V_0^2}. \tag{95}$$

Formally, this condition coincides with the condition of the intersection of the dispersion curves for graphene and its gap modification [44].

5.1.4. The results of the numerical calculation

The numerical calculations of the dependence of the energy on k_x were performed for two values k_y = 0 and 0.1 nm^{-1} at V_0 = 0 (see Fig. 19). The energy of carriers is assumed to be low, $|E| \lesssim 1$ eV, because the Dirac dispersion relation for carriers and, correspondingly, Dirac equation (81) are invalid for high energies.

The electron minibands are separated from hole minibands by a band gap, which increases with $|k_y|$. For $d_I = d_{II}$ at $k_y = 0$, it is $E_g \simeq$ 10–30 meV when d=10–100 nm. In this case, the solution of Eq. (91) is transformed to the solution of Eq. (92). The band gap can increase strongly when d_{II} increases with respect to d_I: $E_g \gtrsim 100$ meV, i.e., is several times larger than $2\Delta_0$.

The width of the minibands decreases with an increase in the period of the superlattice d. The dependence of the width of the minibands on V_0 was also examined. The widths of the electron and hole minibands increase and decrease, respectively, at $V_0 > 0$ and vice versa at $V_0 < 0$.

5.1.5. The possible applications of SL

The described superlattice can be used as FET where the substrate serves as a gate. The ratio of the current through the superlattice to the current through the gate at a substrate thickness of about 10 nm can reach $\sim 10^6$ as for FET based on graphene nanoribbons [11]. The main advantage of the considered superlattice is the absence of the effect of the scattering of carriers on the edges of a nanoribbon on their mobility. The mobility of the carriers in gapless graphene reaches $\mu_0 = 2 \times 10^5$ cm^2/(V s) [4, 5]. However, the mobility of carriers in FET based on the graphene nanoribbon with a width of $w \sim 3$ nm is three orders of magnitude smaller than μ_0. The cause of such a strong decrease is possibly the scattering of carriers at the edges of graphene nanoribbons. The mean free path between two acts of the scattering of carriers at the edge of the graphene nanoribbon $\lambda_{edge} \propto w/P$, where P is the probability of backscattering [11]. For sufficiently good edges, P≪1. The problem of scattering on edges is absent for the proposed superlattice; for this reason, the mobility of the carriers in the superlattice is expected to be $\sim \mu_0$ in the absence of the problems with the periodicity of the potential. At the same time, a sufficiently large E_g value, which provides the operation of FET at room temperature, can be reached.

If an Au film is deposited on the lower side of the substrate and graphene is optically pumped, the superlattice can be used as a terahertz laser similar to a terahertz laser based
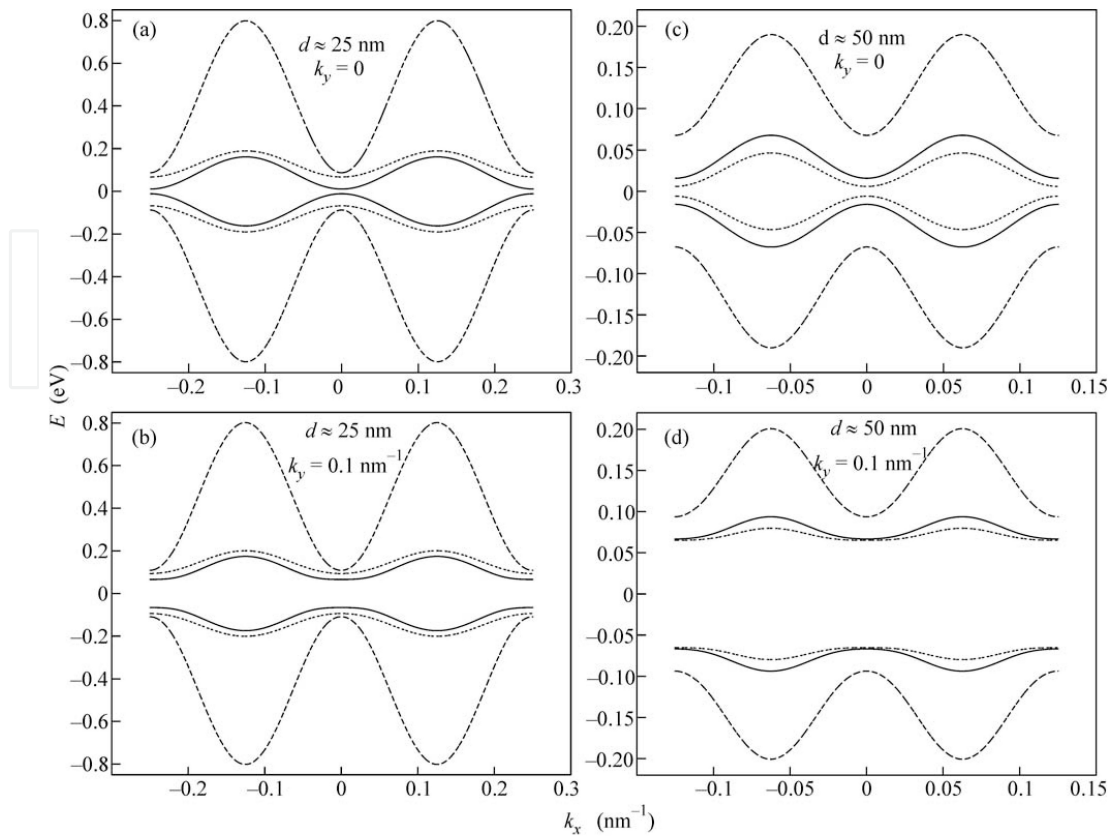
Figure 19. Numerically calculated dependence of the energy on k_x for two k_y values and two superlattice periods d. The dispersion curves for the superlattices with d_I = (solid lines) d_{II}, (dashed lines) $d_{II}/2$, and (dotted lines) $2d_{II}$.

on gapless graphene [89]. In this case, terahertz radiation will be emitted from the regions of the SiO_2 substrate.

5.2. Superlattice based on gapless graphene with the alternating Fermi velocity

5.2.1. Preliminary remarks

Now, we suggest to consider SL based on gapless graphene with alternating regions characterized by different values of the Fermi velocity [90]. In our case, the *Fermi velocity engineering* is based on the usage of the surrounding graphene materials, which have different values of permittivity [91]. It should be pointed out that the idea to control the Coulomb interaction between charge carriers in graphene by the choice of substrate materials with the necessary values of dc permittivity was first put forward in [92].

In such heterostructures, it is possible to achieve the energy quantization for charge carriers even in the absence of potential barriers (regions with wider band gaps) and QWs (regions with narrower band gaps), and even without any variations in the work function [25]. Note that the Tamm minibands are absent here since the straight dispersion lines do not intersect anywhere except for the Dirac point.

Such structure can be produced by the deposition of graphene on striped substrates where either the composition parameter x in an alloy of SiO_{2-x}, or the density of some
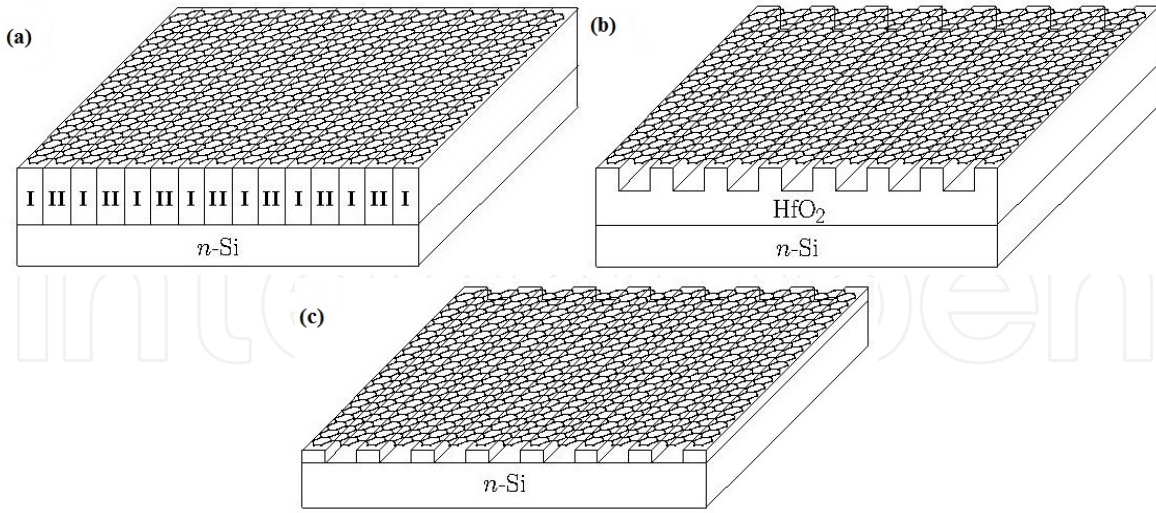
Figure 20. Three variants of SL under study: **(a)** graphene sheet placed on a striped substrate consisting of alternating layers of materials with substantially different values of the permittivity, e.g., SiO$_2$ with $\varepsilon = 3.9$ (I) and HfO$_2$ with $\varepsilon = 25$ (II); **(b)** graphene sheet placed on the HfO$_2$ substrate with periodically arranged grooves; and **(c)** graphene sheet deposited on a periodic array of parallel metallic strips. A plate of heavily doped silicon n-Si is used as a gate.

(nonmagnetic) impurities, or dc permittivity ε exhibit periodic variations. Here, we treat in detail the latter possibility.

According to the results of the theoretical [93–97] and experimental [91, 98–102] studies, the Fermi velocity becomes substantially renormalized. To estimate the renormalized Fermi velocity, we can use the relation [95]

$$\frac{v_F}{v_{F0}} = 1 - 3.28\alpha^* \left[1 + \frac{1}{4} \ln \left(1 + \frac{1}{4\alpha^*} - 1.45 \right) \right],$$

where $\alpha^* = \tilde{e}^2/\hbar v_{F0}$ is the analog of the fine structure constant, v_{F0} is the initial unrenormalized Fermi velocity ($v_{F0} = 0.85 \times 10^8$ cm/s) [91, 101], $\tilde{e}^2 = e^2/\varepsilon_{eff}$, and $\varepsilon_{eff} = (\varepsilon_1 + \varepsilon_2)/2$ is the effective dc permittivity for the charge carriers in graphene depending on the values ε_1 and ε_2 of dc permittivity characterizing the materials surrounding graphene. Note that here the band gap is not open; this is confirmed in experiment with an accuracy of 0.1 meV [101].

Within the graphene region located over the strip with the lower value of ε, we have larger α^*. Hence, the corresponding renormalized Fermi velocity should be higher than that over the strip with the higher value of ε. This suggests the possibility of modulating v_F by varying the substrate permittivity. Note that such a system is a one-dimensional photonic crystal.

The first version of the suggested system is a graphene sheet placed on a striped substrate consisting of alternating layers of materials with substantially different values of the permittivity. A schematic image of such a system is shown in Fig. 20a.

It is also possible to use a substrate with periodically arranged grooves prepared by etching. The graphene sheet placed on such substrate should have the periodically alternating regions
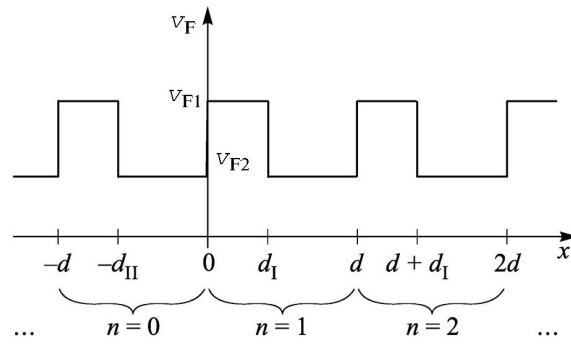
Figure 21. Fermi velocity profile in SL under study ($v_{F1} > v_{F2}$ case). The enumeration of supercells in SL and the sizes of its regions are indicated in the lower part of the figure: d_I is the width of the graphene strip with the Fermi velocity v_{F1}, d_{II} is the width of the graphene strip with the Fermi velocity v_{F2}, and $d = d_I + d_{II}$ is the SL period.

suspended over the grooves and those being in contact with the substrate material (see Fig. 20b). The renormalization of the Fermi velocity should be the most clearly pronounced just in the suspended graphene regions since here we have $\varepsilon_{eff} = 1$. According to the experimental data, the renormalized Fermi velocity in suspended graphene increases to 3×10^8 cm/s [101].

In the regions with graphene in contact with the narrow gap semiconducting material, where $\varepsilon_{eff} \gg 1$, the renormalized Fermi velocity differs only slightly from the unrenormalized one. In addition, the substrate itself is a diffraction grating. Therefore, the system should exhibit rather interesting optical characteristics, demanding a separate study.

There is another version of the system under study. It is possible to deposit graphene on a periodic array of parallel metallic strips (Fig. 20c). This is the limiting case: in the suspended graphene regions, we have $\varepsilon_{eff} = 1$ (the strongest renormalization of the Fermi velocity), whereas in the regions with graphene in contact with metallic strips, we have $\varepsilon_{eff} = \infty$ (vanishing renormalization of the Fermi velocity [91]).

We see that a whole class of such type of systems, which were not studied earlier, is possible. Without doubt, the studies of such systems should lead to important advances in the implementation of the technologies based on the controlled Fermi velocity.

5.2.2. The model

The model for the description of the suggested SL is similar to that used earlier to study SL on the striped substrate with the periodic variation in the band gap [86].

In our case, we assume that the band gap remains unchanged and is equal to zero (gapless graphene) and the work function is the same over all regions of SL (its value is chosen as the energy reference point). We have only a modulation of the Fermi velocity. In gapless graphene, a change in the work function leads to the electrical breakdown and to the creation of electron-hole pairs. We also assume that the near-border region corresponding to the gradual change in the Fermi velocity is much narrower than the SL period. Therefore, the v_F profile can be considered to be sharp enough (see Fig. 21).

We consider the charge carriers located close to the K point of the Brillouin zone (the results should be the same for the charge carriers located in the vicinity of the K' point). Let the x

axis be perpendicular to the strips as is shown in Fig. 21. The envelope of the wave-function $\Psi(x, y)$ for the charge carriers obeys the Dirac-Weyl equation with variable Fermi velocity[7]

$$v_F \boldsymbol{\sigma} \hat{\mathbf{p}} \Psi(x, y) = E\Psi(x, y), \tag{96}$$

$$v_F = \begin{cases} v_{F1}, & d(n-1) < x < -d_{II} + dn \\ v_{F2}, & -d_{II} + dn < x < dn. \end{cases} \tag{97}$$

Here, $\hat{\mathbf{p}} = -i\boldsymbol{\nabla}$ is the momentum operator (here and further on, $\hbar = 1$). Integers n enumerate supercells (see Fig. 21). The Pauli matrices $\boldsymbol{\sigma} = (\sigma_x, \sigma_y)$ act in the space of two sublattices. The motion of charge carriers in SL along the y axis is free; hence, a solution to Eq. (96) has the form $\Psi(x, y) = \psi(x)e^{ik_y y}$.

Similarly to [86, 90], we find a solution of Eq. (96) with respect to $\psi(x)$ for the nth supercell

(i) at $0 < x < d_I$

$$\psi_n^{(1)}(x) = \Omega_{k_1}(x) \begin{pmatrix} a_n^{(1)} \\ c_n^{(1)} \end{pmatrix},$$

$$\Omega_{k_1}(x) = N_{k_1} \begin{pmatrix} 1 & 1 \\ \lambda_+^{(1)} & -\lambda_-^{(1)} \end{pmatrix} e^{ik_1 x \sigma_z},$$

$$\lambda_\pm^{(1)} = \frac{v_{F1}(k_1 \pm ik_y)}{E}, \ k_1 = \frac{\sqrt{E^2 - v_{F1}^2 k_y^2}}{v_{F1}},$$

(ii) at $d_I < x < d$

$$\psi_n^{(2)}(x) = \Omega_{k_2}(x) \begin{pmatrix} a_n^{(2)} \\ c_n^{(2)} \end{pmatrix},$$

$$\Omega_{k_2}(x) = N_{k_2} \begin{pmatrix} 1 & 1 \\ \lambda_+^{(2)} & -\lambda_-^{(2)} \end{pmatrix} e^{ik_2 x \sigma_z},$$

---

[7] In the general case, one should write the anticommutator of the Fermi velocity $v_F(x)$ with the term containing the momentum operator $\hat{p}_x$

$$\frac{1}{2} \{v_F(x), \boldsymbol{\sigma} \hat{\mathbf{p}}\} \Psi(x, y) = E\Psi(x, y).$$

Such symmetrization of the Hamiltonian is necessary for retaining its Hermitian form. Similar problems were considered in [103, 104]. In the case of the stepwise profile (97) of the Fermi velocity, we obtain the equation for $Psi(x, y)$ in form (96). This limitation is not significant since allowance for a smooth dependence $v_F(x)$ will complicate the calculations, but will insignificantly change the final results.
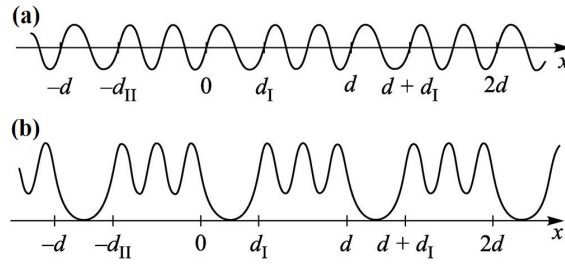
Figure 22. Schematic image illustrating the behavior of the envelope of the wavefunction of charge carriers in SL under study: **(a)** the oscillatory solution in all regions and **(b)** the solution being oscillatory in one region and exhibiting exponential decay deep into another region ($v_{F1} > v_{F2}$ case).

$$\lambda_\pm^{(2)} = \frac{v_{F2}(k_2 \pm i k_y)}{E}, \ k_2 = \frac{\sqrt{E^2 - v_{F2}^2 k_y^2}}{v_{F2}}.$$

Here, N_{k_1} and N_{k_2} are the normalization factors.

For the case $v_{F1} > v_{F2}$, the condition for the existence of the solution of Eq. (96), which oscillates in all regions of the SL (it is schematically illustrated in Fig. 22a), is reduced to the inequality

$$k_2^2 > \left(\frac{v_{F1}^2}{v_{F2}^2} - 1 \right) k_y^2. \tag{98}$$

The existence of a *solution of the mixed type* is also possible (see Fig. 22b). In this case, we have an oscillatory solution in some regions (effective QWs), whereas in the other regions, it exhibits exponential decay (effective potential barriers) deep into these regions. The condition for the existence of the mixed type solution is determined by the inequality inverse to (98) and it is met only for finite k_y values.

The effective quantum barrier of the new type is the region with the higher Fermi velocity because the energy of the charge carriers with the same momentum **k** in it is higher than that in the effective QW with the lower Fermi velocity [25]. In contrast to the usual QW, which is formed owing to the change in the width of the band gap, the height of the barrier in SL under study grows with k_y. At k_y=0, the barrier vanishes and our problem is reduced to the *empty lattice model* [105]. In the latter model, the potential is absent, but the periodicity is retained. As a result, energy bands corresponding to the symmetry of the problem arise, but we have zero band gaps.

5.2.3. The dispersion relation

To derive the dispersion relation, we use the transfer matrix (*T*-matrix) method in the way similar to that employed in [86, 90].

The transfer matrix determines the relation between the coefficients appearing in the expressions for the envelopes of the wavefunctions for the neighboring supercells

$$\begin{pmatrix} a_{n+1}^{(1)} \\ c_{n+1}^{(1)} \end{pmatrix} = T \begin{pmatrix} a_n^{(1)} \\ c_n^{(1)} \end{pmatrix}, \quad \begin{pmatrix} a_{n+1}^{(2)} \\ c_{n+1}^{(2)} \end{pmatrix} = T \begin{pmatrix} a_n^{(2)} \\ c_n^{(2)} \end{pmatrix}.$$

We use the following boundary conditions for matching of the envelopes of the wavefunctions [27, 42]

$$\sqrt{v_{F1}} \psi_n^{(1)} = \sqrt{v_{F2}} \psi_n^{(2)}$$

and also the Bloch conditions in the form

$$\psi_n^{(1)}(x+d) = \psi_n^{(1)}(x) e^{ik_x d}$$

and

$$\psi_n^{(2)}(x+d) = \psi_n^{(2)}(x) e^{ik_x d}.$$

Then, the expression for the T-matrix has the form [86, 90]

$$T = \Omega_{k_1}^{-1}(0) \Omega_{k_2}(d) \Omega_{k_2}^{-1}(d_I) \Omega_{k_1}(d_I).$$

The dispersion relation is determined from Eq. (90), which for the oscillatory type solution, can be written as

$$\frac{v_{F1} v_{F2} k_y^2 - E^2}{v_{F1} v_{F2} k_1 k_2} \sin(k_1 d_I) \sin(k_2 d_{II}) + \cos(k_1 d_I) \cos(k_2 d_{II}) = \cos(k_x d). \tag{99}$$

For the solution of the mixed type, the dispersion relation is found from (99) through the use of the formal substitution $k_1 \to i\kappa_1$, where $\kappa_1 = \frac{1}{v_{F1}} \sqrt{v_{F1}^2 k_y^2 - E^2}$.

At $k_y = 0$, transcendental equation (99) has the form

$$\cos(k_1 d_I + k_2 d_{II}) = \cos(k_x d) \tag{100}$$

for which the exact solution can be found

$$E_l(k_x) = \pm v_F^* \left(k_x + \frac{2\pi l}{d} \right), \quad l = 0, 1, 2, \ldots$$

Here, the effective Fermi velocity is introduced as

$$v_F^* = \frac{v_{F1} v_{F2} d}{v_{F1} d_{II} + v_{F2} d_I}. \tag{101}$$

For the lth miniband, the energy at the K point is equal to

$$E_l^0 = \pm \frac{2\pi l v_F^*}{d}, \ l = 0, 1, 2, \ldots$$

We can see that the lower electron miniband ($l = 0$) touches the upper hole miniband at the K point and graphene remains gapless.

From Eq. (100), we find that, at the edge of the lth miniband, the energy at $k_x = \pm \pi/d$ is equal to

$$E_l \left(\pm \frac{\pi}{d} \right) = \pm \frac{\pi(2l+1)v_F^*}{d}, \ l = 0, 1, 2, \ldots$$

The minibands are separated by the direct band gaps

$$E_G = E_{l+1} \left(\pm \frac{\pi}{d} \right) - E_l \left(\pm \frac{\pi}{d} \right) = \frac{2\pi v_F^*}{d}.$$

In the case of $k_y = 0$, indirect gaps are absent

$$E_l \left(\frac{\pi}{d} \right) = E_{l+1} \left(-\frac{\pi}{d} \right),$$

which corresponds to the empty lattice model [105].

5.2.4. The numerical calculation of the energy spectrum

Let us calculate the lower electron miniband for SL shown in Fig. 19c. According to [101], for it we have $v_{F1} = 3 \times 10^6$ cm/s (suspended graphene) and $v_{F2} = 0.85 \times 10^6$ cm/s (in the region with the contact of graphene with the metal, the Fermi velocity coincides with v_{F0}).

In the weak coupling model, the problem concerning the edge type at the interface turns out to be unimportant. Let us assume that we have a zigzag-type boundary at the interface (see Fig. 20) and, in each of two regions of the supercell, integer numbers N_I and N_{II} of graphene unit cells are packed up. Then, we have $d_I = 3N_I a$ and $d_{II} = 3N_{II} a$, where $a = 1.42$ Å is the lattice constant of graphene. For calculations, we assume that $N_I = N_{II} = 50$, i.e., $d_I = d_{II} = 21.3$ nm.

In the framework of the suggested model, it is necessary to introduce the upper limit on the wave vector component characterizing the free motion of charge carriers, $|k_y| \ll k_c$. Momentum k_c corresponds to the energy of the ultraviolet cutoff, $\Lambda \approx 3$ eV [101]. As a result, we find $k_c \approx 4.3$ nm^{-1}. This, in turn, imposes the limitation on the SL period, $d \gg a$.

The results of numerical calculations are represented in the form of two $E(k_x, k_y)$ plots for the lower electron miniband: (i) $E(k_x)$ at fixed values of k_y (Fig. 23a) and (ii) $E(k_y)$ at fixed values of k_x (Fig. 23b). In Fig. 23a, we can see, in particular, that $k_y = 0$ corresponds to the
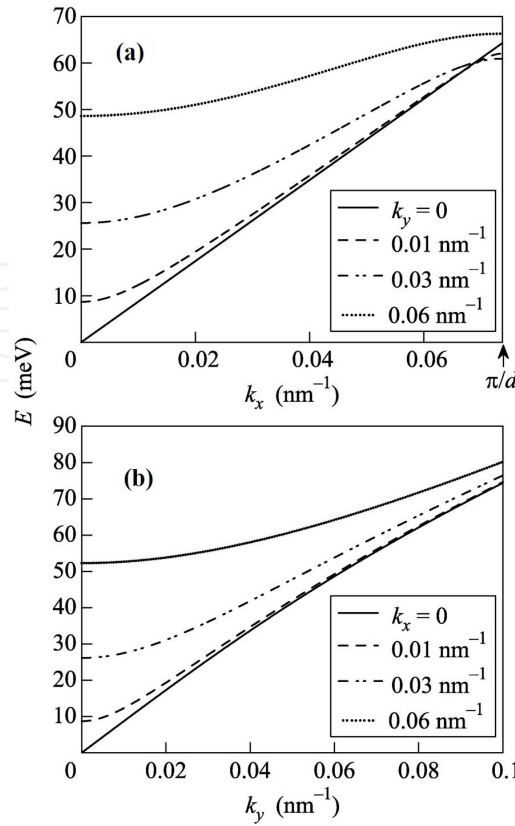
Figure 23. Numerical calculation of the dispersion curves for the lower electron miniband **(a)** versus k_x at fixed k_y values and **(b)** versus k_y at fixed k_x values.

linear dispersion law and the effective Fermi velocity is $v_F^* \approx 1.325 \times 10^8$ cm/s. The lower curve in Fig. 23b exhibits a nearly linear growth. This means that the $E(k_x, k_y)$ surface has the conical shape near the Dirac point.

Thus, we confirm by numerical calculations that at $k_y = 0$, the Fermi velocity of electrons (holes) has a constant value, does not vanish up to the boundaries of minibands, and is determined by Eq. (101) (this is true for all minibands). In this sense, the particles do not feel the boundaries of minibands. Note that, for $k_y \neq 0$, the velocity of particles always vanishes at the miniband boundaries.

5.2.5. The qualitative analysis of the current-voltage characteristics

Let us briefly discuss at the qualitative level the effect of the SL potential on the transport phenomena.

Having in mind the aforementioned qualitative difference between the $k_y = 0$ and $k_y \neq 0$ cases, we should expect that the current-voltage characteristics (*I–V* curves) of SL under study should be significantly different for these two cases.

At $k_y = 0$, the transport characteristics of SL under study should be the same as for effective gapless graphene with the average Fermi velocity v_F^* given by Eq. (101). In particular, at any arbitrarily low charge carrier density, we should observe nonzero minimum conductivity

σ_{min}. According to the experimental data, we have $\sigma_{min} = 4e^2/h$ [2], which coincides with the ballistic conductivity of graphene. The I–V curve should exhibit a linear growth similar to that characteristic of graphene samples with high enough mobility of charge carriers, $\mu \gtrsim 10^4$ cm^2/(V s) [106].

In the case of $k_y \neq 0$, the situation is more complicated. At a nonzero transverse field V_y and at a sufficiently small longitudinal field V_x, the I–V curve should be a growing one and the differential conductivity at small values of V_x is about or higher than the minimum conductivity

$$\sigma_{dif}(V_x \approx 0) \gtrsim \sigma_{min}.$$

Now, we calculate the velocity of electrons for the case of fixed longitudinal ($\mathcal{E}_x$) and nonzero transverse ($\mathcal{E}_y$) electric fields. For the corresponding implementation of such situation in experiment, it is possible to use the standard Hall device.

For simplicity, we assume that transport is ballistic; i.e., the mean free path λ is so large that an electron accelerated by the applied electric field can reach the miniband boundary without any scattering. To distinguish the spectrum related to the potential of the superlattice, the mean free path should be much larger than the period of SL [85]

$$\lambda_f \gg d. \tag{102}$$

For the sufficiently pure graphene samples, we have $\lambda_f \simeq 1\mu$m.

The direction of the electron motion is characterized by the polar angle $\phi = \arctan(k_y/k_x)$. Its value remains unchanged in the whole $-\pi/d \leq k_x \leq \pi/d$ range. The contribution to the conductivity related to the intraminiband transitions is determined by the electron velocity, which we seek:

$$v_\phi = \left.\frac{\partial E}{\partial k}\right|_{k_y = k_x \tan \phi}.$$

In Fig. 24, we illustrate the calculated dependence of the electron velocity on k_x for the same SL parameters as above for the polar angles $\phi = 5^o, 10^o$, and 15°. We can see that the velocity indeed vanishes at the miniband boundary and its abrupt decrease takes place within a quite narrow range near the miniband boundary. For low momenta, we have $v_\phi \approx v_F^*$.

An application of the superlattice at nonzero temperatures requires the existence of a quite clearly pronounced Fermi velocity profile; i.e., we should use rather large ϕ and $\delta v_F = |v_{F1} - v_{F2}|$ values:

$$\pi \frac{\delta v_F}{d} \sin \phi \gg T.$$

However, at large ϕ values close to $\pi/2$, the condition according to which charge carriers pass a large number of supercells at the mean free path can be violated. Then, condition (102) turns out to be unimportant: condition $\lambda_f \cos \phi \gg d$ should be met.
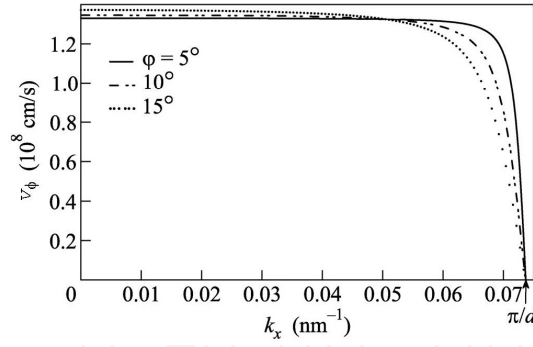
Figure 24. Numerical calculation of the electron velocity in the lower miniband along the direction specified by the fixed polar angle ϕ.

Similarly to the situation occurring in semiconductor SLs, the motion of charge carriers at sufficiently strong electric field $\mathcal{E}_x$ is finite. They oscillate with the Stark frequency [85]

$$\Omega = e\mathcal{E}_x d.$$

This stems from the nonlinearity of the I–V curve manifesting itself in the negative differential conductivity at a certain section of it. Charge carriers in the nonlinear regime undergo a large number of the Bloch oscillations during the mean free time τ:

$$\Omega\tau \gg 1. \tag{103}$$

We estimate the mean free time as $\tau \approx \lambda_f / v_F^*$ (the velocity of charge carriers is $v_\phi \approx v_F^*$ everywhere except for a narrow range near the miniband boundaries). Then, condition (103) can be rewritten as

$$\mathcal{E}_x \gg \frac{v_F^*}{ed\lambda_f}. \tag{104}$$

Condition (104) automatically gives an estimate for the minimum longitudinal voltage above which negative differential conductivity becomes possible

$$V_{x\,\text{min}} \simeq \frac{v_F^*}{ed}\frac{L_x}{\lambda_f},$$

where L_x is the size of the system along the x axis. Assuming that $L_x \simeq \lambda_f$, we arrive at the estimate $V_{x\,min} \simeq 0.02$ V for SL with the same parameters as above.

In Fig. 25, we represent the qualitative behavior of the I–V curve for SL under study. At $k_y = 0$ (zero applied voltage in the transverse direction, $V_y = 0$), we observe its linear growth. At $k_y \neq 0$ (nonzero transverse voltage, $V_y \neq 0$), a section with negative differential conductivity arises in the curve. In this case, for higher V_y values, this section is more pronounced and more shifted toward lower V_x values. However, as is mentioned above, this section can arise only at a sufficiently high longitudinal voltage
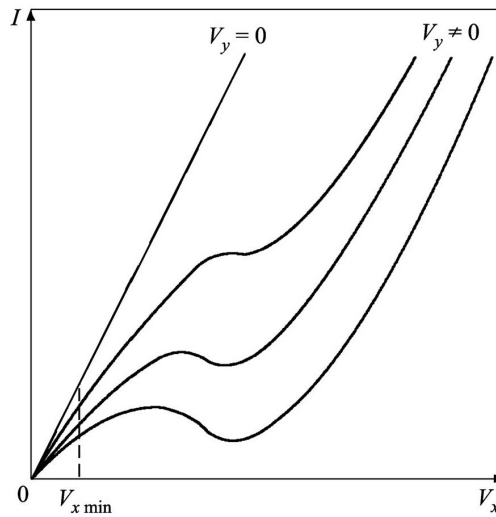
Figure 25. Qualitative behavior of the I–V curve for SL under study. Three $I(V_x)$ plots under the linear I–V curve correspond to the growth of the transverse voltage V_y (from top to bottom).

$$V_x \gg V_{x\,\min}.$$

Note finally that the characteristics of the system under study can depend on the gate voltage V_g (at different values of the charge carrier density n_{2D}) owing to the dependence of the renormalized Fermi velocity on n_{2D} [101, 102]. In this case, a controlling factor is the filling of minibands with electrons (holes). For the experimental observations, it is convenient to have partially filled either the lower electronic miniband or the upper hole one (in this case, the higher electronic or lower hole minibands are distinguishable). This takes place if $n_{2D} \ll n_{2D}^* = 4/d^2$. This condition can be rewritten in the form of a limitation imposed on the gate voltage [90]

$$|V_g| \ll 4\pi e n_{2D}^* L_g / \varepsilon_s^*,$$

where L_g is the gate thickness and ε_s^* is the effective dc permittivity of the substrate. For the layered substrate structure (see Fig. 19a), we have

$$\varepsilon_s^* = \frac{\varepsilon_{s1} d_I + \varepsilon_{s2} d_{II}}{d}.$$

6. Conclusions

We presented the method for the theoretical research of the electron properties of the planar heterostructures based on graphene, namely, the single heterojunctions, QWs, and SLs. The usage of the gap modifications of graphene in the planar heterostructures is a novel idea which can help to push the boundaries of science.

The valley-polarized currents must exist at the single heterojunctions. The novel phenomena of pseudospin splitting in the energy spectrum of the asymmetric QWs had been theoretically predicted. Some optical properties of the graphene-based QWs was considered (observation of the excitonic lines).

A model describing SL based on graphene on a strip substrate has been proposed. The dispersion relation has been derived, which is transferred to the known nonrelativistic dispersion relation in the passage to the single-band limit. The numerical calculations have been performed for a pair of the nearest electron and hole minibands using the derived dispersion relation. Possible applications of SL as a transistor or a terahertz laser have been pointed out.

We suggested a novel class of graphene-based systems, which are at the same time both photon crystals and graphene SLs with periodically varying Fermi velocity. Such a modulation appears to be possible owing to the renormalization of the Fermi velocity in the energy spectrum of graphene. New prospects become open for the implementation of the technologies based on controlled Fermi velocity. We point out some specific features of the transport phenomena in such systems, in particular, appearance of the sections with negative differential conductivity in the $I-V$ curves. It is clear that, similarly to photon crystals, these systems should exhibit interesting optical characteristics.

Author details

Pavel V. Ratnikov* and Andrei P. Silin

*Address all correspondance to: ratnikov@lpi.ru

Lebedev Physical Institute, Russian Academy of Sciences, Moscow, Russia

References

[1] K.S. Novoselov, A.K. Geim et al., Science **306**, 666 (2004).

[2] K.S. Novoselov, A.K. Geim et al., Nature **438**, 197 (2005).

[3] Y. Zhang, Y.-W. Tan, H. L. Stormer, and P. Kim, Nature **438**, 201 (2005).

[4] S.V. Morozov, K.S. Novoselov et al., Phys. Rev. Lett. **100**, 016602 (2008).

[5] X. Du, I. Skachko, A. Barker, and E.Y. Andrei, Nat. Nanotech. **3**, 491 (2008).

[6] L. Brey and H.A. Fertig, Phys. Rev. B **73**, 235411 (2006).

[7] L. Brey and H.A. Fertig, Phys. Rev. B **75**, 125434 (2007).

[8] Y.-W. Son, M.L. Cohen, and S.G. Louie, Phys. Rev. Lett. **97**, 216803 (2006).

[9] R. Saito, G. Dresselhaus, and M.S. Dresselhaus, *Physical Properties of Carbon Nanotubes* (Imperial College Press, London, 1998).

[10] T. Ando, J. Phys. Soc. Jpn. **74**, 777 (2005).

[11] X. Wang, Y. Ouyang et al., Phys. Rev. Lett. **100**, 206803 (2008).

[12] L.A. Ponomarenko, F. Schedin et al., Science **320**, 356 (2008).

[13] J. Y. Tan, A. Avsar et al., Appl. Phys. Lett. **104**, 183504 (2014).

[14] Y.-C. Lin, C.-Y.S. Chang et al., Nano Lett. **14**, 6936 (2014).

[15] Y.F. Lin, W. Li et al., Nanoscale **6**, 795 (2014).

[16] D. Logoteta, G. Fiori, and G. Iannaccone, Scientific Rep. **4**, 6607 (2014).

[17] B.G. Idlis and M.Sh. Usmanov, Sov. Phys. Semicond. **26** (2), 186 (1992).

[18] A. I. Akhiezer and V. B. Berestetskii, *Quantum Electrodynamics* (Wiley, New York, 1965; Nauka, Moscow, 1969).

[19] A.H. Castro Neto, F. Guinea et al., Rev. Mod. Phys. **81**, 109 (2009).

[20] Yu.E. Lozovik, S.P. Merkulova, and A.A. Sokolik, Phys.–Usp. **51** (7), 727 (2008).

[21] S.S. Schweber, *Introduction to Relativistic Quantum Field Theory* (Halper and Row, New York, 1961).

[22] A.M. Tsvelik, *Quantum Field Theory in Condensed Matter Physics* (Cambridge University Press, 1998).

[23] T.W. Appelquist, M. Bowick, D. Karabali, and L.C.R. Wijewardhana, Phys. Rev. D **33**, 3704 (1986).

[24] B.A. Volkov, B.G. Idlis, and M.Sh. Usmanov, Phys.–Usp. 38 (7), 761 (1995).

[25] A.V. Kolesnikov and A.P. Silin, JETP **82**, 1145 (1996).

[26] A.V. Kolesnikov and A.P. Silin, J. Phys.: Condens. Matter **9**, 10929 (1997).

[27] A.P. Silin and S.V. Shubenkov, Phys. Solid State **40** (7), 1223 (1998).

[28] E.A. Andryushin, Sh.U. Nutsalov, and A.P. Silin, Phys. Low-Dim. Struct. **7/8**, 85 (1999).

[29] E.A. Andryushin, S.A. Vereshchagin, and A.P. Silin, Kratk. Soobshch. Fiz., No. 6, 21 (1999).

[30] E.A. Andryushin, A.P. Silin, and S.A. Vereshchagin, Phys. Low-Dim. Struct. **3/4**, 85 (2000).

[31] A.P. Silin and S.A. Vereshchagin, Phys. Low-Dim. Struct. **9/10**, 115 (2001).

[32] E.A. Andryushin, Sh.U. Nutsalov, and A.P. Silin, Kratk. Soobshch. Fiz., No. 3, 3 (2001).

[33] P.V. Ratnikov and A.P. Silin, Kratk. Soobshch. Fiz., No. 11, 22 (2005).

[34] G.W. Semenoff, Phys. Rev. Lett. **53**, 2449 (1984).

[35] D.A. Abanin, P.A. Lee, and L.S. Levitov, Phys. Rev. Lett. **96**, 176803 (2006).

[36] P.V. Ratnikov and A.P. Silin, Phys. Solid State **52** (8), 1763 (2010).

[37] G. Giovannetti, P.A. Khomyakov et al., Phys. Rev. B **76**, 073103 (2007).

[38] A. Mattausch and O. Pankratov. Phys. Rev. Lett. **99**, 076802 (2007).

[39] S.Y. Zhou, G.-H. Gweon et al., Nature Mater. **6**, 770 (2007).

[40] D.C. Elias, R.R. Nair et al., Science **323**, 610 (2009).

[41] S. Lebègue, M. Klintenberg, O. Eriksson, M.I. Katsnelson. Phys. Rev. B **79**, 245117 (2009).

[42] P.V. Ratnikov and A.P. Silin, JETP **114**, 511 (2012).

[43] G. Tkachov. Phys. Rev. B **79**, 045429 (2009).

[44] A.V. Kolesnikov, R. Lipperheide, A.P. Silin, U. Wille. Europhys. Lett. **43**, 331 (1998).

[45] Y. Kobayashi, K.I. Fukui et al., Phys. Rev. B **71**, 193406 (2005).

[46] Y. Niimi, T. Matsui, et al., Phys. Rev. B **73**, 085421 (2006).

[47] S.Y. Zhou, G.-H. Gweon et al., Nature Phys. **2**, 595 (2006).

[48] I. Zanella, S. Guerini et al., Phys. Rev. B **77**, 073404 (2008).

[49] S. Marchini, S. G*ü*nther, and J. Witterlin, Phys. Rev. B **76**, 075429 (2007).

[50] D. Martoccia, P.R. Willmon et al., Phys. Rev. Lett. **101**, 126102 (2008).

[51] I. Pletikosić, M. Kralj et al., Phys. Rev. Lett. **102**, 056808 (2009).

[52] M.Y. Han, B. Özyilmaz, Y. Zhang, and P. Kim, Phys. Rev. Lett. **98**, 206805 (2007).

[53] T.M. Rice, J.C. Hensel, T. Phillips, and G.A. Thomas, *The Electron-Hole Liquid in Semiconductors: Theoretical Aspects* (Academic, New York, 1977; Mir, Moscow, 1980).

[54] A.A. Abrikosov, J. Low Temp. Phys. **2**, 37 (1970).

[55] S.A. Brazovskii, Sov. Phys. JETP **35** , 433 (1972).

[56] T. Ando, J. Phys. Soc. Jpn. **66**, 1066 (1997).

[57] V.S. Babichenko, L.V. Keldysh, and A. P. Silin, Sov. Phys. Solid State **22** (4), 723 (1980).

[58] Yu.E. Lozovik and V.I. Yudson, Phys. Lett. **56A**, 393 (1976).

[59] L.V. Keldysh, JETP Lett. **29** (11), 658 (1979).

[60] R. Loudon, Am. J. Phys. **27**, 649 (1959).

[61] A. Dalgarno and J.T. Lewis, Proc. R. Soc. A **233**, 70 (1955).

[62] D.A.B. Miller, D.C. Chemla et al., Phys. Rev. Lett. **53**, 2173 (1984).

[63] E.I. Rashba, Sov. Phys. — Solid State **2**, 1109 (1960).

[64] Yu.A. Bychkov and E.I. Rashba, JETP Lett. **39** (2), 78 (1984).

[65] Yu.A. Bychkov and E.I. Rashba, J. Phys. C: Solid State Phys. **17**, 6039 (1984).

[66] D. Graf, F. Molitor et al., Nano Lett. **7**, 238 (2007).

[67] Z.H. Ni, W. Chen et al., Phys. Rev. B **77**, 115416 (2008).

[68] A.C. Ferrari, J.C. Meyer et al., Phys. Rev. Lett. **97**, 187401 (2006).

[69] I. Calizo, A.A. Balandin et al., Nano Lett. **7**, 2645 (2007).

[70] L.A. Chernozatonskii, P.B. Sorokin et al., JETP Lett. **84**, 115 (2006).

[71] L. A. Chernozatonskii, P. B. Sorokin et al., JETP Lett. **85**, 77 (2007).

[72] A. Isacsson, L.M. Jonsson, J.M. Kinaret, and M. Jonson, Phys. Rev. B **77**, 035423 (2008).

[73] F. Guinea, M.I. Katsnelson, and M.A.H. Vozmediano, Phys. Rev. B **77**, 075422 (2008).

[74] T.O. Wehling, A.V. Balatsky, M.I. Katsnelson, and A.I. Lichtenstein, Europhys. Lett. **84**, 17003 (2008).

[75] C. Bai and X. Zhang, Phys. Rev. B **76**, 075430 (2007).

[76] M. Barbier, F.M. Peeters, P. Vasilopoulos, and J.M. Pereira, Phys. Rev. B **77**, 115446 (2008).

[77] C.-H. Park, L. Yang et al., Phys. Rev. Lett. **101**, 126804 (2008).

[78] C.-H. Park, Y.-W. Son et al., Nano Lett. **8**, 2920 (2008).

[79] M.R. Masir, P. Vasilopoulos, A. Matulis, and F.M. Peeters, Phys. Rev. B **77**, 235443 (2008).

[80] M.R. Masir, P. Vasilopoulos, and F.M. Peeters, Phys. Rev. B **79**, 035409 (2009).

[81] L. Dell'Anna and A. De Martino, Phys. Rev. B **79**, 045420 (2009).

[82] S. Ghosh and M. Sharma, J. Phys. Condens. Matter **21**, 292204 (2009).

[83] H. Sevinçli, M. Topsakal, and S. Ciraci, Phys. Rev. B **78**, 245402 (2008).

[84] S.Y. Zhou, G.-H. Gweon et al., Nature Mater **6**, 770 (2007).

[85] A. P. Silin, Sov. Phys. Usp. **28**, 972 (1985).

[86] P.V. Ratnikov, JETP Lett. **90**, 469 (2009).

[87] M.A. Herman, *Semiconductor Superlattices* (Academy, Berlin, 1986; Mir, Moscow, 1989).

[88] G.M. Maksimova, E.S. Azarova, A.V. Telezhnikov, and V.A. Burdov, Phys. Rev. B **86**, 205422 (2012).

[89] V.Ya. Aleshkin, A.A. Dubinov, and V. Ryzhii, JETP Lett. **89**, 63 (2009).

[90] P.V. Ratnikov and A.P. Silin, JETP Lett. **100**, 311 (2014).

[91] C. Hwang, D.A. Siegel et al., Sci. Rep. **2**, 590 (2012).

[92] P.V. Ratnikov, JETP Lett. **87**, 292 (2008).

[93] J. Gonzalez, F. Guinea, and M.A.H. Vozmediano, Nucl. Phys. B **424**, 595 (1994).

[94] J. Gonzalez, F. Guinea, and M.A.H. Vozmediano, Phys. Rev. B **59**, 2474 (1999).

[95] S. Das Sarma, E.H. Hwang, and W.-K. Tse, Phys. Rev. B **75**, 121406(R) (2007).

[96] M.S. Foster and I.L. Aleiner, Phys. Rev. B **77**, 195413 (2008).

[97] F. de Juan, A.G. Grushin, and M.A.H. Vozmediano,Phys. Rev. B **82**, 125409 (2010).

[98] A. Bostwick, T. Ohta et al., Solid State Commun. **143**, 63 (2007).

[99] Z.Q. Li, E.A. Henriksen et al., Nature Phys. **4**, 532 (2008).

[100] G. Li, A. Luican, and E.Y. Andrei, Phys. Rev. Lett. **102**, 176804 (2009).

[101] D.C. Elias, R.V. Gorbachev et al., Nature Phys. **7**, 701 (2011).

[102] J. Chae, S. Jung et al., Phys. Rev. Lett. **109**, 116802 (2012).

[103] M.R. Geller and W. Kohn, Phys. Rev. Lett. **20**, 3103 (1993).

[104] A.V. Kolesnikov and A.P. Silin, Phys. Rev. B **95**, 7596 (1999).

[105] J. Callaway, *Energy Band Theory* (Academic, New York, 1964; Mir, Moscow, 1969).

[106] N. Vandecasteele, A. Barreiro et al., Phys. Rev. B **82**, 045416 (2010).